Engineering Structures 345 (2025) 121496

Contents lists available at ScienceDirect

Engineering Structures

journal homepage: www.elsevier.com/locate/engstruct

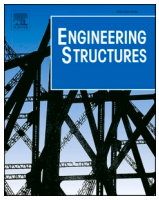

3D-printed multi-functional sinusoidal metamaterials for simultaneous vibration isolation and electricity generation

Ramin Hamzehei [a], Mahdi Alaei Varnosfaderani [b], Mahdi Bodaghi [c,*], Nan Wu [a,*]

[a] Department of Mechanical Engineering, University of Manitoba, Winnipeg, Manitoba, R3T 5V6, Canada
[b] Department of Civil Engineering, University of Manitoba, Winnipeg, Manitoba, R3T 5V6, Canada
[c] Department of Engineering School of Science and Technology, Nottingham Trent University, Nottingham NG11 8NS, UK

ARTICLE INFO

Keywords:
Sinusoidal metamaterials
Vibration isolation
Quasi-zero stiffness
3D printing
Piezoelectric materials
Electricity generation
Stability

ABSTRACT

This study introduces 3D-printed multi-functional sinusoidal metamaterials designed for simultaneous vibration isolation and electricity generation. The innovative design follows the sinusoidal patterns derived from re-engineered common auxetic re-entrant unit cells, resulting in multi-stiffness lattice structures. Layers of unit cells, with one rotated 90°, are integrated, facilitating local buckling in the vertical beams under compression. A quasi-zero-stiffness (QZS) mechanism, achieved through local buckling-induced nonlinearity, is incorporated to enhance vibration isolation. Two stabilizers are designed to maintain global structural stability under compression and dynamic loads, and the underlying deformation mechanisms are elucidated by finite element analysis (FEA) and experiments. Experimental evaluation reveals effective vibration isolation for frequencies above 15 Hz. For electricity generation, two piezoelectric materials are employed, namely Lead zirconate titanate (PZT) and piezo bender (PB). The flexible lattice structure, made from thermoplastic polyurethane (TPU), can withstand substantial bending deformations under a specific load and simultaneously apply bending forces to the PB. This leads to electricity generation at approximately 3 volts (V) and maximum generated power around 700 microwatts per gravity ($\frac{\mu W}{g}$) by one PB at a low frequency of 15 Hz, where vibration isolation arises. Meanwhile, one PZT, mounted on a polylactic acid (PLA)-based semi-honeycomb structure, generates energy due to higher dynamic forces caused by high-stiffness property of PLA, leading to electricity generation at around 500 millivolts (mV), and a maximum generated power of 800 $\frac{\mu W}{g}$ at a high frequency of 90 Hz. The proposed metamaterials exhibit material-independent properties with multi-functional potentials for simultaneous vibration isolation and electricity generation. They support wearable applications, enabling motion tracking and injury prevention in protective gear through self-powered sensing. In civil structures, these hybrid metamaterials can be embedded in bridge joints, isolation pads, or foundations to reduce low-frequency vibrations and power wireless sensors for real-time, self-sustained structural health monitoring.

1. Introduction

Mechanical metamaterials are engineered structures whose unique mechanical properties derive from the specific geometric design of their unit cells [1]. Indeed, the internal geometrical design can significantly affect mechanical properties such as stiffness, resonance behavior, and fatigue life [2]. In addition, they exhibit more extraordinary mechanical characteristics, including negative mechanical indices such as negative Poisson's ratio [3, 4], negative stiffness [5, 6], negative thermal expansion [7–9], and tunable mechanical properties like adjustable stiffness [10]. These features could not typically be found in conventional materials and structures. By tailoring the geometry of unit cells, mechanical metamaterials can be customized for diverse applications, including energy absorption/dissipation [11, 12], vibration isolation [13, 14], sound absorption [15, 16], impact resistance [17, 18], and energy generation [19–22], making them versatile for fields ranging

Abbreviations: QZS, Quasi-zero stiffness; NS, Negative stiffness; NPR, Negative Poisson's ratio; 2D, Two-dimensional; ω_n, Natural angular frequency; ω, Excitation angular frequency; $\frac{\omega}{\omega_n}$, Frequency ratio; ζ, Damping ratio; M, Mass of the system; K, Stiffness of the system; TPU, Thermoplastic polyurethane; PB, Piezo bender; PZT, Lead zirconate titanate; FFT, Fast Fourier transform; G, Acceleration due to gravity; W, Watt unit of power.

* Corresponding authors.
E-mail addresses: mahdi.bodaghi@ntu.ac.uk (M. Bodaghi), nan.wu@umanitoba.ca (N. Wu).

https://doi.org/10.1016/j.engstruct.2025.121496
Received 6 June 2025; Received in revised form 25 August 2025; Accepted 27 September 2025
Available online 3 October 2025

from aerospace to automotive engineering [23].

Mechanical metamaterials can be categorized into two main groups, called passive and active metamaterials [24]. Passive metamaterials are those whose unique mechanical properties arise solely from their structural design and intrinsic material composition, requiring no external energy input to function. When it comes to the active behavior of metamaterials, the role of smart materials is hard to ignore [25]. They are substances that respond to external stimuli such as temperature, pressure, electric fields, or magnetic fields by altering their physical properties in a controlled manner. They include shape-memory polymers /alloys [26, 27]' which can return to a pre-defined shape after deformation via an external stimulus like heating. Another example could be magnetorheological compounds [28], which change viscosity under magnetic fields.

Piezoelectric materials [29, 30], which generate an electric charge in response to mechanical stress, are another important class of smart materials. The work by Alshenawy et al. [31] employed a three-dimensional strain gradient formulation combined with the moving Kriging meshfree method to analyze the nonlinear stability of functionally graded piezoelectric micro shells under coupled mechanical, thermal, and electrical loading, providing insights relevant to the design of multi-field responsive metamaterial systems. Similarly, Gao et al. [32] developed a perforated metamaterial plate integrated with acoustic black holes interconnected by piezoelectric studs, enabling broadband vibration suppression and directional flexural wave manipulation through tunable bandgaps and collimation effects. Another example showing the power of piezo materials was achieved by Zhu et al. [33]. They introduced a hybrid triboelectric–piezoelectric nanogenerator-based intelligent pipeline clamp system for aero-engine applications, capable of harvesting energy from pipeline vibrations while simultaneously enabling self-powered monitoring and fault diagnosis. Likewise, Liu et al. [34] investigated nonlinear buckling mode transitions in functionally graded piezoelectric nanoshells under thermo-electromechanical loading using a nonlocal couple stress-based numerical model with the moving Kriging meshfree method, offering new insights into stability enhancement at the nanoscale. When these materials are combined with passive mechanical metamaterials, a new class of multi-functional active metamaterials can react and adapt to their environment.

From the mechanical point of view, mechanical vibration [35] is the oscillatory motion of an object around a stable equilibrium condition. This mechanical behavior is heavily dependent on the stiffness and the corresponding natural angular frequency of a system defined as $\omega_n = \sqrt{\frac{k}{m}}$, where "$\omega_n$" is denoted the natural angular frequency of a system, "k" is stiffness, and "m" is the system's mass respectively. According to the natural angular frequency formula, stiffness affects the natural angular frequency of a system directly. It can take values ranging from positive to negative. A system with PS behavior resists deformation when an external force is applied. Indeed, the system generates a restoring force in the opposite direction of the applied displacement. For the high value of "K", the natural angular frequency is a positive value, meaning that the higher the stiffness, the higher the natural angular frequency. On the flip side, in a system with NS behavior, the force acts in the same direction as the displacement is applied, which facilitates deformation. It is also worth mentioning that a system with QZS behavior has no resistance to displacement. Another key concept regarding mechanical vibration is frequency ratio, defined as the ratio of $\frac{\omega}{\omega_n}$. Fig. 1 shows a typical frequency response curve of a second-order differential equation system with different values of the damping ratio, ζ. When the effective stiffness of a system decreases and approaches zero, the natural angular frequency goes to zero. Indeed, by shifting stiffness from a positive value to a zero or even negative value, a softening behavior can be achieved by effectively lowering the natural angular frequency towards zero. Then, the frequency ratio goes to infinity, and the magnitude response becomes very low. This implies that the system effectively isolates vibrations at low frequencies.

Vibration isolation of mechanical metamaterials, as a key aspect of vibration control, has been extensively reviewed by Ji et al. [36]. In this regard, Wu et al. [37] developed an elastic metamaterial beam incorporating X-shaped local resonators to achieve broadband vibration attenuation. Amendola et al. [38] investigated the nonlinear elastic response of layered penta-mode metamaterials confined between stiffening plates, demonstrating their potential for seismic isolation. Matlack et al. [39] developed composite 3D-printed elastic meta structures that combine local resonances with structural modes of a periodic lattice to achieve wide and low-frequency band gaps while maintaining low mass. Amongst different kinds of mechanical metamaterials, those employing QZS designs are increasingly explored for their potential in vibration isolation [40–49]. Zhang et al. [40] developed a new class of tailored mechanical metamaterials featuring programmable QZS characteristics using curved beam geometries, enabling multiple QZS regions for ultra-low frequency vibration isolation through a material-independent mechanism. Liu et al. [41] designed a compact and lightweight design of

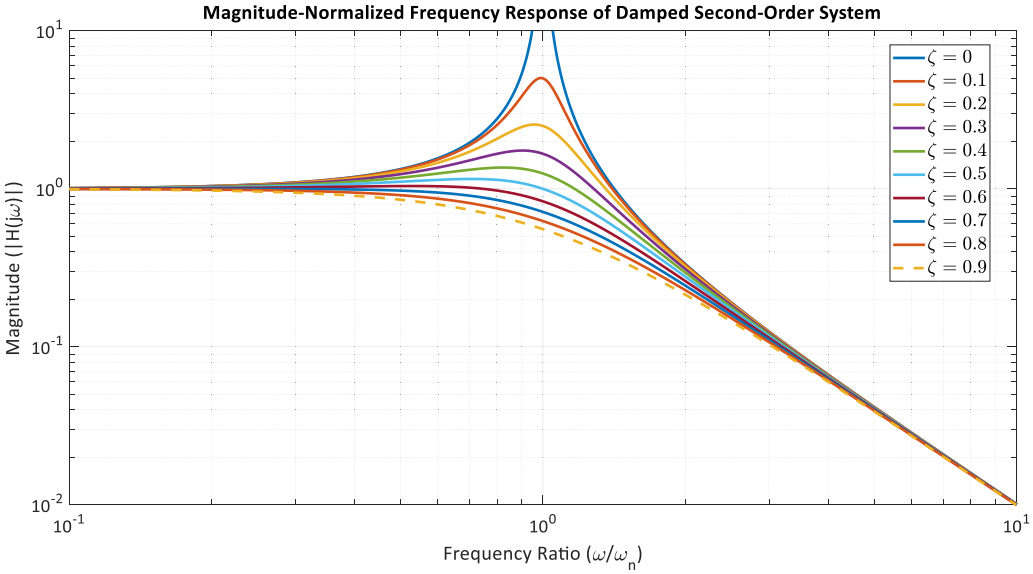

Fig. 1. Typical frequency response curve of a second-order differential equation system at different damping ratios.

representative unit cells combining positive stiffness (heart-shaped beam) and negative stiffness (cosine beam) for low-frequency broadband vibration isolation. Liu et al. [42] designed "meta springs" with a modular approach to achieve customizable QZS behavior for low-frequency vibration isolation. The mechanism integrates optimized unit cells with tailored stiffness characteristics, enabling programmable QZS behavior. Liang et al. [43] designed a novel vibration isolation metamaterial featuring a broad QZS platform by integrating horizontal and diagonal beams based on Euler buckling and flexural deformation mechanisms. The design leverages negative stiffness components mitigated by supportive structures, enabling tunable, multi-stage vibration isolation across a wide displacement range. Liu et al. [44] designed origami-inspired QZS metamaterials using Kresling-pattern structures combined with a decoupling strategy, enabling multi-directional low--frequency vibration isolation in both vertical and lateral directions. Dalela et al. [45] designed a tunable QZS metamaterial based on a single elastically deformable beam, eliminating the need for combined positive and negative stiffness elements. Their innovative approach leveraged the buckling behavior of the beam to achieve QZS characteristics for low-frequency vibration isolation. Huo et al. [46] designed a programmable low-frequency isolator using QZS metamaterials, incorporating Euler cosine beams and elastic buckling mechanisms. Their design enabled tunable vibration isolation, effectively addressing nonlinear dynamic responses for micro-vibration isolation. Zhao et al. [47] developed a lightweight and compact metastructure for vibration isolation, employing a monolithic curved beam design to achieve a QZS feature. Their design integrated tunable geometric parameters for customizable load-carrying capacity and broadband vibration isolation. Zhou et al. [48] designed a multi-layer QZS meta-structure for low-frequency vibration isolation, utilizing flexible multi-segment beams. Their design relied on a stackable architecture of single-layer units, showcasing enhanced vibration isolation performance with increasing layers while maintaining ease of assembly. Fan et al. [49] designed a metastructure for vibration isolation that achieves a QZS feature by integrating sinusoidal beams exhibiting snap-through behavior with semicircular arches providing bending-dominated positive stiffness.

Each of the above studies focuses on specific mechanisms such as combining positive and negative stiffness elements, magnetic systems, utilizing origami-inspired folding patterns for tunable stiffness, and employing modular or stackable unit cells to extend the isolation range and tunability. However, many of these mechanisms may exhibit a lack of structural stability, which becomes critical when it comes to applying dynamic loads to a structure. Stability is particularly important for maintaining performance under varying loads and dynamic excitations, where designs without sufficient lateral or vertical supports may exhibit instability.

Mechanical metamaterials have also been used for electricity generation applications, so-called energy harvesting [50–58]. Chen et al. [50] designed a gradient auxetic piezoelectric energy harvester that integrates a cantilever beam with gradient auxetic structures to enhance power output. By creating a more uniform strain distribution and reducing stress concentration, the gradient auxetic design achieved a 356 % and 55 % increase in power density compared to conventional and uniform auxetic energy harvesters, respectively. Li et al. [51] designed a piezoelectric bimorph with a 2D auxetic structure showing NPR behavior to enhance energy harvesting efficiency. This mechanism increased transverse stress, enabling simultaneous engagement of both 31- and 32-modes, resulting in an increase of 2.76 times in power output compared to conventional bimorphs. Farhangdoust et al. [52] designed a novel metamaterial-based substrate combining auxetic and kirigami structures to enhance energy harvesting efficiency. This design utilized the interplay of auxetic expansion and kirigami cuts to achieve multi-directional strain distribution. This led to an increase of 19.2 times higher power output compared to conventional harvesters under low-frequency and low-strain conditions. Fey et al. [53] designed a 2D piezoelectric auxetic lattice structure using PZT ceramics with a re-entrant hexagonal geometry. The design demonstrated significant enhancements in piezoelectric coupling coefficients and strain responses compared to bulk PZT, offering potential for advanced sensor and actuator applications. Eghbali et al. [54] designed piezoelectric vibration energy harvesters enhanced by auxetic booster structures, amplifying strain and stress in piezoelectric layers. Their design showed an increase in power output by up to 10.43 times compared to conventional harvesters. Ferguson et al. [55] designed an auxetic piezoelectric energy harvester by incorporating a re-entrant honeycomb auxetic structure into the substrate to enhance power output. This mechanism concentrates stress and introduces NPR behavior in the piezoelectric element, increasing power output by up to 14.4 times compared to conventional designs. Chen et al. [56] designed an enhanced nonlinear piezoelectric energy harvester by integrating a clamped–clamped beam with multiple rotating square auxetic unit cells. This mechanism amplifies stress and expands the operating bandwidth by improving power output by an increase of 268 % and a 14 % broader bandwidth compared to conventional harvesters. Ichige et al. [57] designed a piezoelectric vibration energy harvester incorporating a mechanical metamaterial elastic layer, with a tunable periodic structure to reduce resonance frequency and increase power output. They achieved a 16 % reduction in resonance frequency and a 100 % increase in power generation compared to conventional designs.

While several studies have explored vibration isolation and enhanced energy harvesting using lattice structures, challenges remain in achieving higher output voltages and maintaining structural stability under dynamic loads. Moreover, most research has focused on energy harvesting of cantilever beam designs for lattice structures, which can restrict the integration of multiple piezoelectric patches. In parallel, a few studies have been carried out on multi-functional lattice structures for simultaneous vibration isolation and electricity generation [14, 59–62]. This research delves into the design and fabrication of multi-functional sinusoidal metamaterials for simultaneous vibration isolation and electricity generation applications. The struts of the common auxetic re-entrant unit cell are reformulated by a sinusoidal pattern with different curvatures, resulting in multi-stiffness sinusoidal elements. The lattice structures were fabricated from TPU due to their excellent flexibility in handling bending deformations under compression. To achieve an excellent vibration isolation feature, the QZS feature is introduced to the system via local buckling of the vertical struts of the unit cells. Indeed, the common re-entrant unit cell exhibiting high-stiffness property is used to provide global stability for the whole structure, and its sinusoidal counterparts, showing low-stiffness property used in a rotated position of 90° relative to the other layer to facilitate the local buckling of the vertical struts. For electricity generation, PB is attached inside (through depth) of the lattice structure. Due to significant bending deformations caused by the local buckling of the vertical struts, an electricity generation of around 3 volts (V) and maximum generated power around 700 microwatts per gravity ($\frac{\mu W}{g}$) at the frequency of 15 Hz, where vibration isolation arises, was achieved. It is worth mentioning that the generated voltage and power are just related to one attachment of PB, and multiple PBs can be integrated within the lattice structure for higher voltage and power generation. PZT is also used at the base of the semi-honeycomb lattice structure, which is placed on a shaker. Once the shaker applies external excitations, higher forces are applied to the PZT, resulting in electricity generation around 500 millivolts (mV), and a maximum generated power of 800 $\frac{\mu W}{g}$ at a high frequency of 90 Hz.

2. Material & methods

2.1. Lattice structure design

This study considers the traditional re-entrant unit cell referred to as

"A". Then, the straight ligaments of the unit cell are replaced with sinusoidal ligaments with varying curvatures, "B", and "C" [11,12], see Fig. 2***a***. The wall thickness of model "A" unit cell is 1 mm, 0.9 mm wall thickness for model "B", and 0.8 mm of wall thickness for model "C". To provide stability for the structure once a mass is placed on the top, two hybrid designs consisting of unit cells "A" and "C" are considered, called "V-structure" to provide stability for multi layers of the rotated unit cell "C", and "H-structure" to provide stability for a single layer of the rotated unit cell "C", see Figs. 2***b*** and 2***c***. For "V-structure", if the support columns are too tall, contact may occur between the object placed on the rotated part "C" and the columns. This leads to transmitting vibration directly to the object from the columns, reducing the vibration isolation effect. If the columns are too short, the object placed on the rotated part "C" may become unstable during external excitation. Indeed, the chosen height gives a balance between stability and isolation. For "H-structure", the base support tolerates the bending momentum applied from the buckled struts of rotated "C" models. If the length of the base support is the same as the single rotated part "C", instability may occur while an object is placed on a single rotated layer of part "C", in particular when external excitation is applied. Therefore, the base support for "H-structure" should be large enough to ensure stability. It is also worth noting that for both designs "H" and "V", transitional buffers, composed of curve design "C" and showing low stiffness property, are strategically placed between the top head and foundation as the low-stiffness connections to reduce the transmission of vibration from the stiff load paths into the rotated low-stiffness part "C", which tolerates the object. The

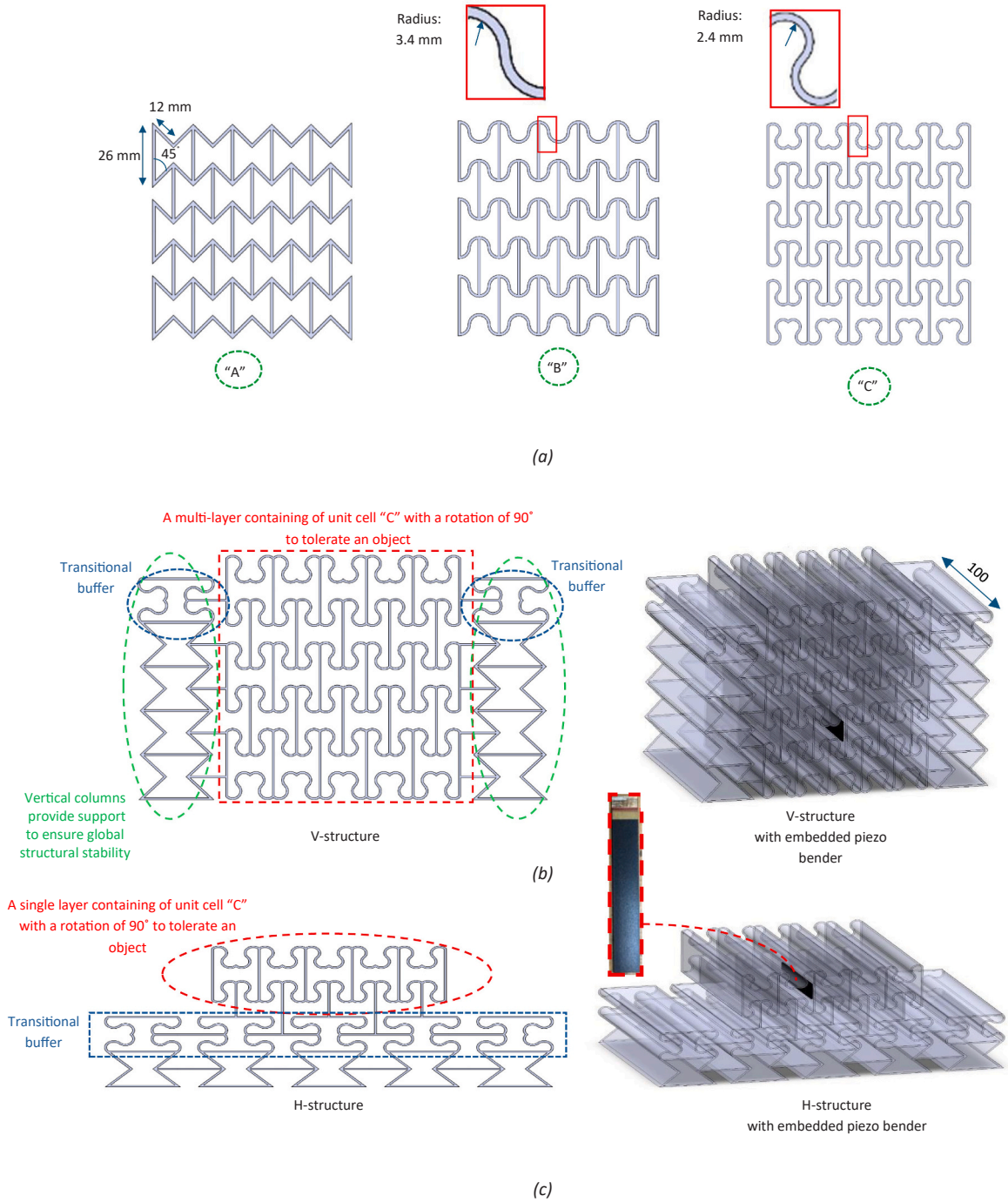

Fig. 2. ***(a)*** Common and sinusoidal structures "A", "B", "C", hybrid design with stability provided for ***(b)*** multi-layer, and ***(c)*** single layer of unit cell "C".

depth of all non-hybrid and hybrid structures is 100 mm. The reasons and corresponding deformation mechanisms, features behind selecting model "C" for the introduction of QZS property, vibration isolation feature, and the design of hybrid structures to ensure stability will be elucidated in the results and discussion section via FEA and experiments.

2.2. Material and fabrication

This study uses TPU as a hyperelastic material [63] for fabrication, characterized by its ability to undergo large elastic deformations and return to its original shape upon removing the applied load. The main reasons for the selection of TPU are related to its flexibility to handle significant bending deformations. To achieve the mechanical properties of TPU, five dog-bone samples were additively manufactured according to the standard ASTM-D-638–14 [64], see Fig. 3***a***. Tensile tests were carried out by MTS universal testing machine at a speed of 50 $\frac{mm}{min}$, see Fig. 3***a***. The stress-strain curves of TPU are provided in Fig. 3***b***. For the fabrication of the samples in this study, the Bambu Lab X1 carbon machine was employed with the following setup, see Table 1. As TPU is a hyperelastic material and may exhibit strain rate dependency at different mechanical conditions, tensile tests at different speeds of 50, 200, and 500 $\frac{mm}{min}$ were carried out. Based on the experimental data provided in Fig. 3***c***, in the low to moderate strain range (0–0.5), which corresponds to the operational regime for vibration isolation under small cyclic displacements, the response is nearly rate-independent. This validates its suitability for vibration isolation testing in this research, where displacement amplitudes and frequencies remain within the domain of small-to-moderate strain.

Table 1
Printing parameters.

Printing parameters	Value
Nozzle diameter	0.4 mm
Nozzle temperature	250C
Bed temperature	30C
Printing speed	50 $\frac{mm}{s}$
Infill direction	$\pm$ 45
Infill percentage	100 %

2.3. Finite element analysis (FEA)

The quasi-static mechanical response of the proposed hybrid "V" and "H" lattice structures was simulated using the ABAQUS finite element software. The sixth-order Ogden model was adopted as the hyperelastic constitutive model. The analysis was conducted in two sequential steps: a "linear perturbation buckling" step, followed by a "general static Riks" step. In the buckling analysis, a subspace eigensolver was employed to extract the first five eigenmodes. The first buckling mode was subsequently introduced as a geometric imperfection into the structure for the "Riks" step to capture post-buckling and nonlinear deformation behavior. To implement this imperfection, the buckling mode shapes must first be linked to nodal displacements by adding the following two lines to the model keywords:

*Node file
U

The model is then duplicated in ABAQUS, and the analysis step is changed from "Buckle" to "Static, Riks". After removing the previously added lines, the following command is inserted to apply the imperfection:

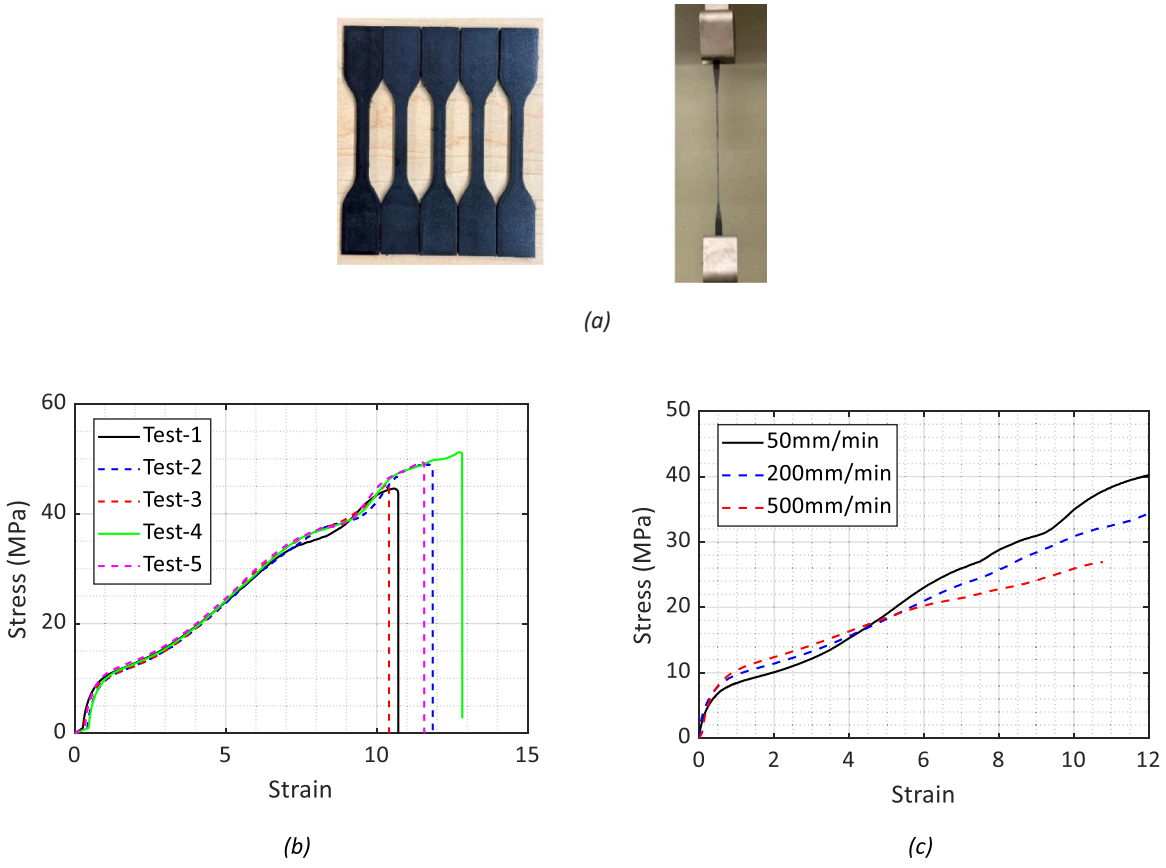

Fig. 3. ***(a)*** 3D-printed TPU samples with corresponding tensile test, ***(b)*** stress-strain curves of TPU at 50 $\frac{mm}{min}$, and ***(c)*** strain independence behavior of TPU at different speeds.

*Imperfection, File=Buckle analysis job-name, Step= 1
1, scale-factor
where scale-factor represents a small value (For example, 0.01–0.1) used to scale the first buckling mode shape.

For boundary conditions, the movement of the bottom faces of the structures is restricted along the horizontal and vertical directions, and a 15 mm displacement is applied to the top faces, see Fig. 4. The simulations utilized "C3D8RH" elements, 8-node linear bricks with reduced integration, hybrid formulation, and hourglass control. This element is ideal for modelling nearly incompressible materials like TPU, ensuring numerical stability during large deformations. The hybrid formulation handles pressure constraints effectively, making it suitable for buckling and post-buckling analyses using static "Riks", while reduced integration improves computational efficiency. It is worth noting that a mesh seed size of 0.4 mm, corresponding to half the wall thickness, was used to ensure FEA accuracy, as illustrated in Fig. 11 and 12.

2.4. Experimental set-up

The experimental procedure in this study relies on three main experiments, including a quasi-static compression test to evaluate the stiffness and the QZS property of all lattice structures. Then, a vibration test is carried out to evaluate the vibration isolation behavior of hybrid lattice designs "V-structure" and "H-structure", and simultaneously, the amount of generated voltage by PB and PZT is measured. The details regarding each step are provided in the following subsections.

2.4.1. Quasi-static compression test

To evaluate the mechanical properties of the proposed metamaterials, a quasi-static compression test was carried out at a speed of 5 $\frac{mm}{min}$ via the MTS universal testing machine, see Fig. 5.

2.4.2. Vibration test

A vibration test was carried out via acoustic shaker "Ling Dynamic Systems (LDS)" with a frequency range of 0–100 Hz, see Fig. 6. The data acquisition and signal generation system contain a four-channel Siemens LMS SCADAS Mobile integrated with LMS Test Lab software, showing a schematic of the signal generator and data acquisition system, see Fig. 7. The signal generator produces the required AC voltage, which is then amplified and applied to the shaker. For harmonic signals, we directly used the amplifier, while for periodic chirp signals, the LMS system generated the signal, which was then applied to the amplifier. The LMS system is configured to measure the outputs: the first channel measures PB voltage, the second channel measures PZT voltage, the third channel measures base plate acceleration, and the fourth channel measures top plate acceleration. Accelerations of the base and top plates are captured by two accelerometers, which send the data to the LMS system for analysis.

Fig. 5. Quasi-static compression test.

Fig. 6. LDS shaker used in vibration tests.

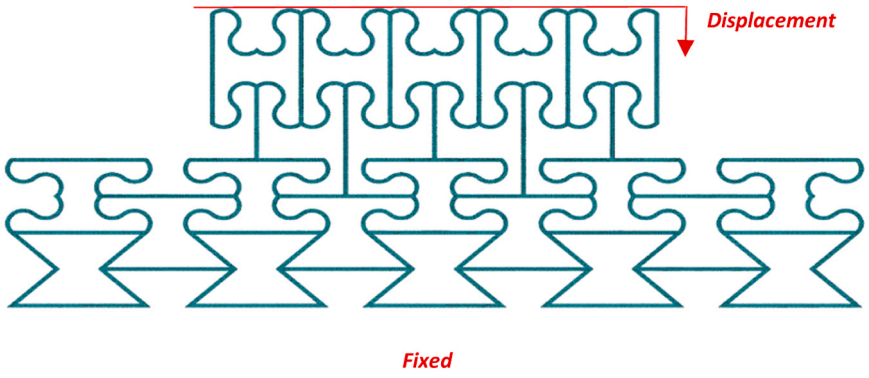

Fig. 4. The meshed structure with corresponding boundary conditions.

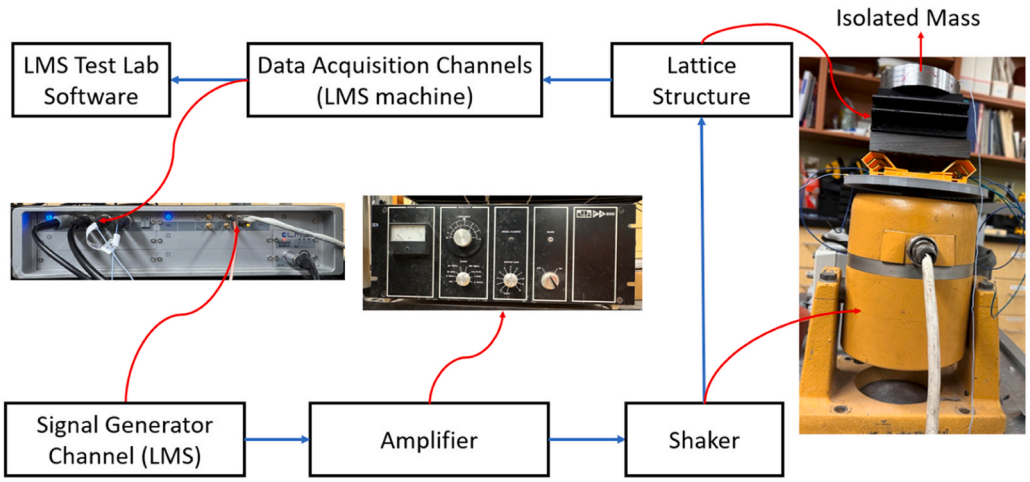

Fig. 7. Signal Generator and Data Acquisition System.

2.4.3. Energy generation test

We employed two piezoelectric materials for energy generation: PB and PZT. Regarding PB, it is directly attached to the lattice cell wall at a point where the maximum bending deformation is observed. PB is a BA5010 piezoelectric bimorph actuator [65] with a dimension of 50 × 10 × 0.8 mm with a capacitance of 50.84 nF. It is indeed a piezoelectric bimorph configured in parallel poling. These actuators can be wired in either a two-wire or three-wire configuration. For energy generation purposes, we used the two-wire configuration, with the ground connected to the top and bottom electrodes (external surfaces) and the voltage lead connected to the middle plate. In this setup, we used the actuator in reverse, functioning as an energy generator instead of its typical actuation role. Instead of generating energy through the usual out-of-plane bending along the length of the bender (50 mm), energy is generated from the in-plane bending along its width (10 mm), where the lattice structure undergoes local bending. This generates voltage and induces electric fields along with the thickness (polling direction) of PB. As shown in Fig. 8, the "V-structure" contains more sinusoidal unit cells, and PB is positioned closer to the base where more external excitation exists. In contrast, the "H-structure" has fewer unit cells, and PB is located closer to the top. It will be shown that multiple PBs can be embedded within the metamaterials, read Section 3.1.2.2.

Regarding PZT, two PZTs with a dimension of 40 × 30 × 4 mm with a capacitance of 8.78 nF are embedded in a PLA-based semi-honeycomb structure, see Fig. 9. PZTs were fixed and glued to the semi-honeycomb PLA-based structure. Two wires were used to measure the generated voltage across the top and bottom electrodes of the PZTs. It should be highlighted that there are three PLA-based semi-honeycomb supports at the base for stability, see Fig. 8. Although all semi-honeycomb supports can hold PZTs, only the middle support contained PZTs, and data was recorded from this unit just for one PZT due to the symmetrical design of the PLA-based semi-honeycomb support. A heavy metal plate was placed on top of the PLA support to exert additional force on the PZT to generate higher voltage under dynamic loads.

2.4.4. Theoretical maximum generated power

In synchronized energy generation systems, energy extraction is coordinated with the mechanical motion of the piezoelectric transducer. Specifically, energy is ideally extracted at each voltage peak, occurring twice per vibration cycle, once during the positive half-cycle and once during the negative half-cycle. The energy stored in the piezoelectric energy generator at each peak is calculated as follows.

$$E_{PEH} = \frac{1}{2} C_p V_{\max}^2 \tag{1}$$

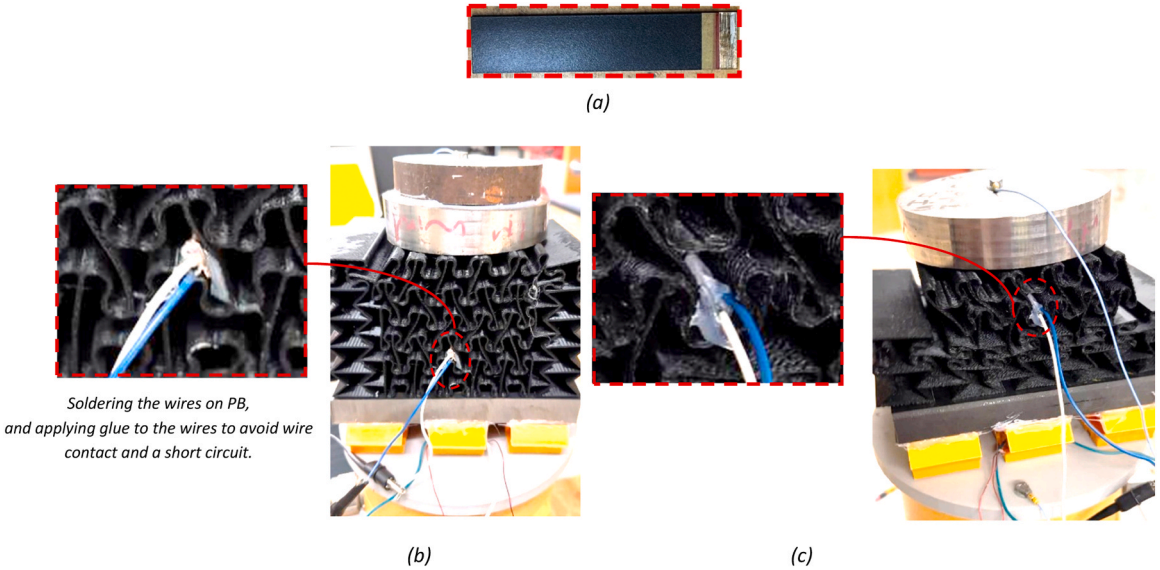

Fig. 8. (a) PB, **(b)** V-structure, and **(c)** H-structure with corresponding experimental setup.

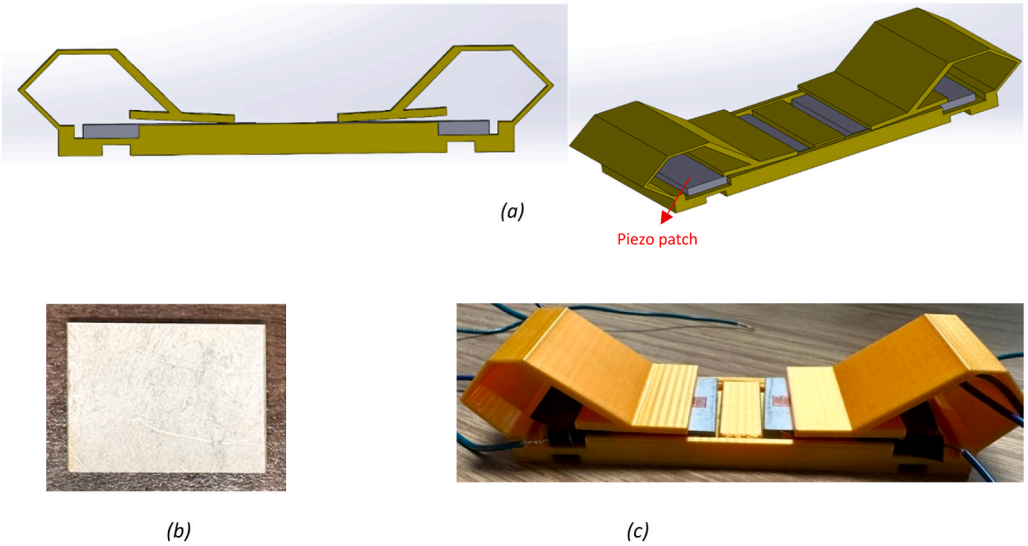

Fig. 9. **(a)** Front and 3D views of PLA-based semi-honeycomb structure, **(b)** PZT, and **(c)** fabricated PLA-based support with embedded PZTs.

Where C_p and $V_{\max}$ are the capacitance and the peak voltage of the piezoelectric, respectively. Assuming the system is being excited at a frequency of f (the number of cycles per second is f). Therefore, the maximum average power (also referred to as raw power) that can theoretically be extracted from the piezoelectric generator is as follows [66].

$$P_{PEH,\max} = f.2 \times E_{PEH} = C_p f V_{\max}^2 \tag{2}$$

3. Results & discussion

The results are presented in two separate sections, reporting the lattice structure deformation patterns under quasi-static compression first, and then vibration isolation and energy generation of the proposed designs under dynamic loads.

3.1. Quasi-static compression test

3.1.1. Non-hybrid structures "A", "B", and "C"

The quasi-static compression behavior of lattice structures is investigated in this section. The geometrical designs and experimental procedure follow the contents mentioned in Sections 2.1 and 2.4.1. According to Fig. 10***a***, model "A" shows a layer-by-layer collapse under quasi-static compression. This leads to snap-through behavior after yield, and multiple plateau regions in the force-displacement relation, see Fig. 10***d***. On the flip side, when it comes to sinusoidal designs "B" and "C", more uniform deformation patterns occur during compression. However, there is a key difference between models "B" and "C." In model "B," the structural stiffness changes from positive to negative, exhibiting an unstable equilibrium path and a snap-through behavior, see Fig. 10***d***. This results in the appearance of a neat plateau region with a quasi-constant force feature after the limit point, specifically less than 16 Newtons (N). Consequently, for forces greater than 16 N, the structural behavior transitions through the plateau region, making it impossible to attribute the behavior of model "B" to an exact QZS feature. In contrast, model "C" with its higher curvature in the sinusoidal struts, experiences a quasi-stable equilibrium path and does not exhibit a snap-through behavior. The higher curvature design leads to earlier dense and supports during structural deformation, especially when the vertical supports buckle. The absence of snap-through behavior allows model "C" to experience a pure QZS feature with a lower level of quasi-constant force. In other words, the negative stiffness behavior of models "A" and "B" is related to the geometric nonlinearity and local buckling of the straight vertical struts. Under axial compression, bending moments concentrate in the junction regions between the vertical struts and the inclined connecting members. These junctions act as stress/strain concentration zones, and once the local bending capacity is exceeded, they behave like rotational hinges. This hinge formation triggers a rapid configuration change (snap-through), releasing stored strain energy and causing a temporary drop in force. As a result, model "C" can be a better choice than model "B" for applications requiring QZS features and effective vibration isolation behavior.

3.1.2. Why hybrid structures?

As discussed in Section 3.1.1, the unit cell "C" can be a better choice for vibration isolation behavior compared to unit cells "A" and "B" due to exhibiting a pure QZS property after yield. Therefore, unit cell "C" is considered for designing hybrid structures. The design of hybrid structures is motivated by the cross-based buckling behavior observed in model "C", see Fig. 10***c***. However, due to the high curvature unit cell design and the low-stiffness property of model "C", when a free mass sits on top, the structure leans easily. When a dynamic excitation is applied, the whole structure experiences a stability problem and can not provide stable support to the mass. To ensure structural stability, two hybrid designs, "V" and "H", are proposed, and the underlying deformation mechanisms will be elucidated through the FEA and experiments.

3.1.2.1. Hybrid structure "V". One approach to enhance stability is to introduce vertical supports for the low-stiffness sinusoidal parts, see Fig. 2***b***. This assembly method allows for the inclusion of more low-stiffness unit cells between two high-stiffness vertical columns. However, under compression, the lateral constraints imposed by the surrounding high-stiffness components restrict the deformation and bending of the low-stiffness sinusoidal elements located in the vicinity of the vertical columns. To shed more light on the structural stability, Fig. 11***a*** provides deformation mechanisms and corresponding stress

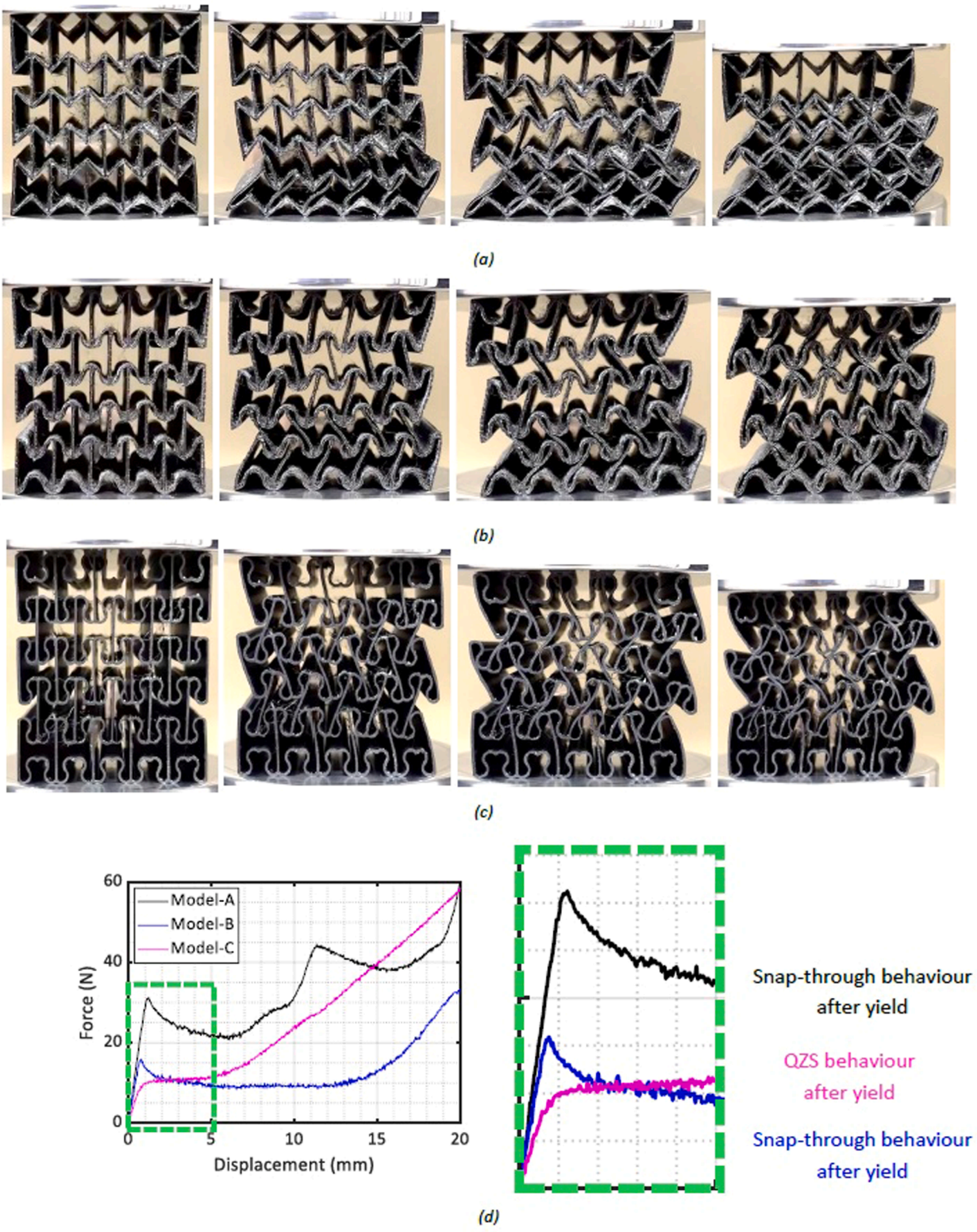

Fig. 10. Deformation patterns of lattice structures ***(a)*** "A", ***(b)*** "B", ***(c)*** "C", and ***(d)*** the corresponding force-displacement relation.

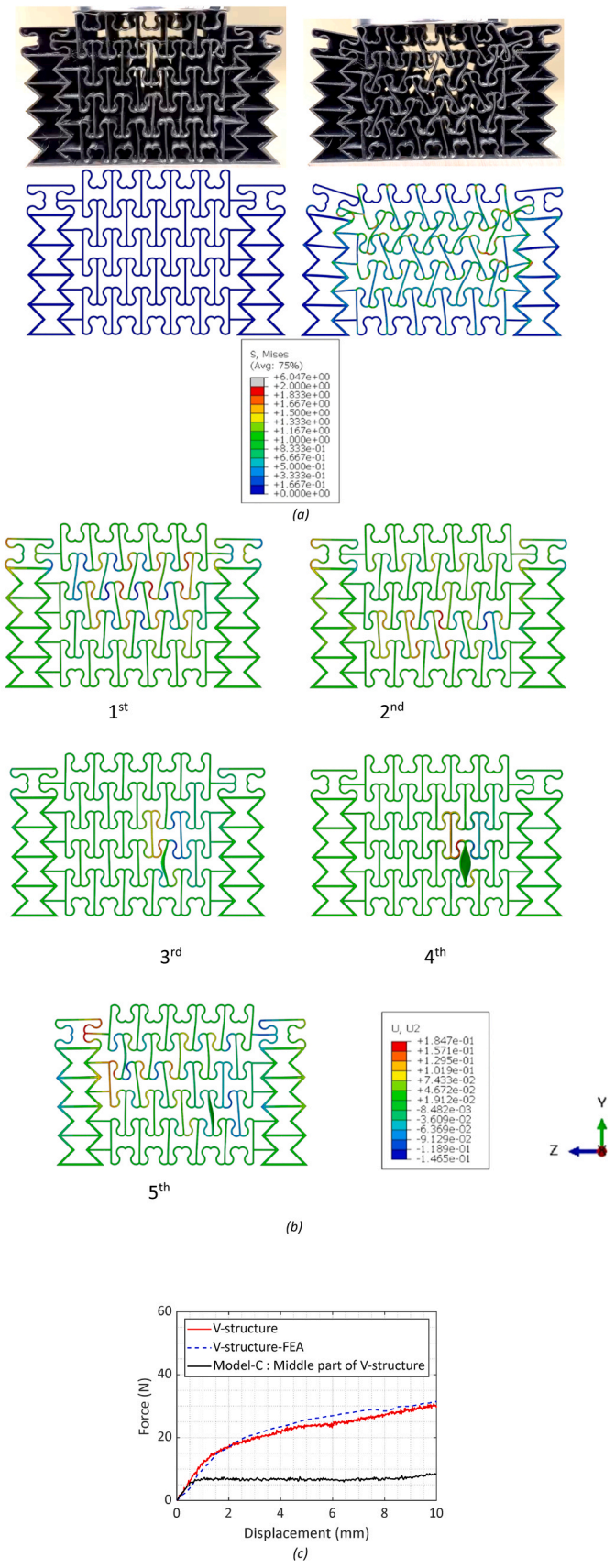

Fig. 11. ***(a)*** Deformation patterns and corresponding stress distribution contour in the hybrid structure "V", ***(b)*** Buckling mode shapes of the hybrid structure "V" with corresponding displacement contour, and ***(c)*** the corresponding force-displacement relation obtained from the FEA and experiment.

propagation contour under compression. Upon compression, stress is primarily concentrated in the sinusoidal elements "C" due to their lower stiffness compared to the common unit cells "A". Consequently, under a constant applied mass, the common unit cells "A" experience lower stress levels and help maintain global structural stability, while the sinusoidal unit cells "C" undergo localized buckling to accommodate deformation. In fact, the top layer bends and rotates first once compression is applied, while showing instability. Once the side walls (transitional buffers) of this top layer contact with the rotated unit cells "C", they cannot bend much further, so the load is passed down to the next layer of "C" cells. As a result, although there is a reduction in structural stiffness under compression, the global response of the "V-structure" does not exhibit a pure QZS feature due to the movement restrictions applied by the vertical columns. However, it could tolerate heavier masses due to the vertically high-stiffness supports. Fig. 11***c*** shows this point by exhibiting a pure QZS behavior by the sole unit "C" and structural stiffness reduction when it is restricted by vertical high-stiffness columns in the "V-structure". For further investigation of the deformation mechanism of the hybrid structure "V", firstly, the first five buckling mode shapes are extracted from ABAQUS, see Fig. 11***b***. They reveal that deformation primarily initiates within the low-stiffness sinusoidal unit cells "C", while the common unit cells "A" remain largely unaffected. This behavior indicates that the sinusoidal elements possess lower bending stiffness, making them more susceptible to local buckling. The presence of the common unit cell "A" helps maintain the global integrity of the structure, even local instabilities occur in sinusoidal regions. This division of mechanical roles contributes to the overall structural stability by localizing buckling and preventing undesired global collapse. Small differences between the simulation and experiment, such as stress levels or the exact spot where deformation begins, are mainly due to the imperfections of the numerical model and printing quality. However, the overall deformation patterns and structural responses between simulations and experiments are in promising agreement.

3.1.2.2. Hybrid structure "H". Another effective stability approach is to incorporate a large supporting foundation with a greater number of high-stiffness unit cells (model "A") horizontally compared to low-stiffness unit cells (model "C") in the structure, see Fig. 2***c***. Indeed, the QZS feature arises due to cross-buckling behavior in multi-layers of "C" as shown in Fig. 10***c and d***, and because of the low-stiffness feature of "C" design, the pure model "C" itself cannot tolerate the mass on top while external excitation is applied from the bottom, see Fig. 12***a***. To realize the structural stability under dynamic excitations and dig into the main reasons behind proposing the hybrid structure "H', a single layer of "C" is printed, and its mechanical properties are compared with the hybrid counterpart. As can be seen from Fig. 12***b and d,*** although the single layer exhibits good stability with solid support after compression, it is incapable of displaying cross-buckling behavior and the corresponding QZS feature. The feedback force slightly drops in a small displacement range (<2 mm). Therefore, it necessitates the proposal of a hybrid design "H", see Fig. 12***c***, with an orthogonal foundation to make good use of the solid support of a single layer "C" while allowing multi-directional struts' degree of freedom to exhibit local cross-buckling behavior without much restriction. It is worth noting that while embedding the hard piezo-materials may affect the local stiffness of the lattice, the provided response of the "H-structure" embedded with six PBs in Fig. 12***d*** shows the same mechanical response under compression but with a slight increase in force value at high compressive displacement due to an earlier densification caused by PBs' thicknesses. Therefore, the QZS property in this research is not affected by embedding multiple PBs. Fig. 12***e*** presents the first five buckling mode shapes of the hybrid structure "H" under compression. By comparing these with the experimental results shown in Fig. 12***c***, it can be inferred that the structure buckles primarily according to the first mode shape,

(a)

(b)

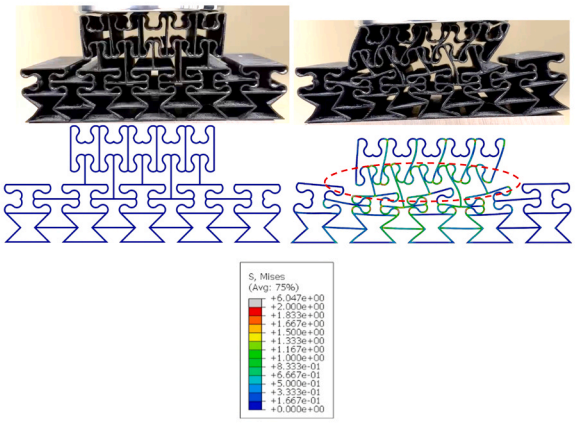

(c)

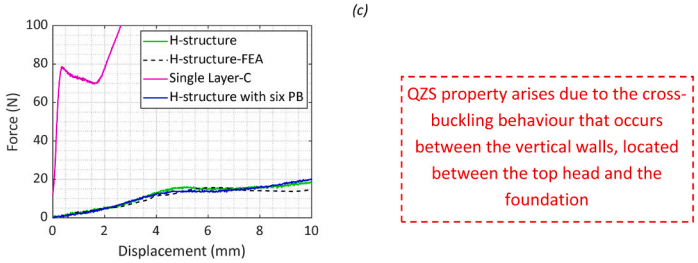

(d)

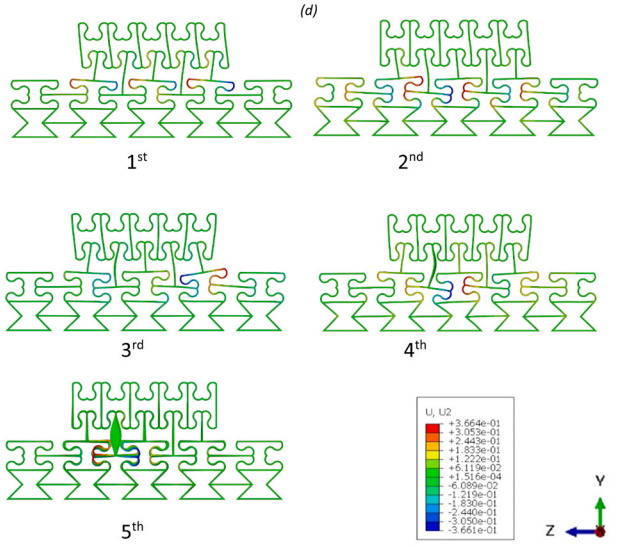

(e)

Fig. 12. ***(a)*** instability problem of pure model "C" structure, ***(b)*** Single-layer of "C" deformation patterns, ***(c)*** deformation patterns and corresponding stress distribution contour in hybrid structure "H", ***(d)*** the corresponding force-displacement relation, and ***(e)*** Buckling mode shapes of hybrid structure "H" with corresponding displacement contour.

corresponding to the lowest energy configuration.

3.2. Vibration isolation & energy generation

This section sheds light on the vibration behavior and energy generation of the hybrid lattice structures. To characterize the system's dynamic behavior, we estimate the transfer functions by using the base plate acceleration, "g", as the input, the top plate acceleration, piezoelectric voltages and maximum average power as the outputs, dividing the FFT results of the outputs by the input. Estimating transfer functions helps in understanding how the structure responds to vibrations across the frequency spectrum, which is critical for applications like vibration control and energy generation. Finally, we apply the signal at specific frequencies to analyze the time-domain responses, providing insight into how the system behaves under different vibration conditions in real-time. It is worth mentioning that the selection of a mass to place on top of the structures for QZS property comes from Fig. 11***c*** ***and*** 12***d***. Therefore, 1.5 and 2 Kilograms of mass are considered to be on top of the "H-structure" and "V-structure", respectively. In the following sections, experimental vibration isolation and electricity generation results regarding each structure are presented. In the supplementary document, Videos S1 and S2 show the vibration isolation of "H" and "V" structures, respectively.

Supplementary material related to this article can be found online at doi:10.1016/j.engstruct.2025.121496.

3.2.1. V-structure

Fig. 13 presents the transfer functions of the "V-structure", with the base plate acceleration "g" as the input, upper plate acceleration (Fig. 13***a***), the piezoelectric voltages (Fig. 13***b***), and maximum average power (raw power) (Fig. 13***c***) as outputs. According to Fig. 13***a***, the lattice structure effectively dampens vibrations beyond 15 Hz, where the transfer function drops below one ($|T_a(f)| < 1|$). It is worth noting that there is a rise in transmissibility starting at approximately 90 Hz is attributed to the structural dynamics of the system. This frequency range is close to one of the natural frequencies of the structure, where resonance effects become significant. Additionally, Fig. 13***b*** and Fig. 13***c*** show that the PB is more effective than the PZT in voltage and maximum average power below 15 Hz. The reason is related to the reasonable vibration isolation behavior of the lattice structure beyond 15 Hz, where oscillations in the cell walls decrease, hence, bending forces required for PB to generate electricity are reduced. However, after 15 Hz, where vibration isolation arises, the PZT's voltage and power output gradually increase, while the PB's output decreases. Around 53 Hz, the PZT surpasses the PB in voltage output, while the generated power remains comparable, suggesting a divergence in voltage behavior without a

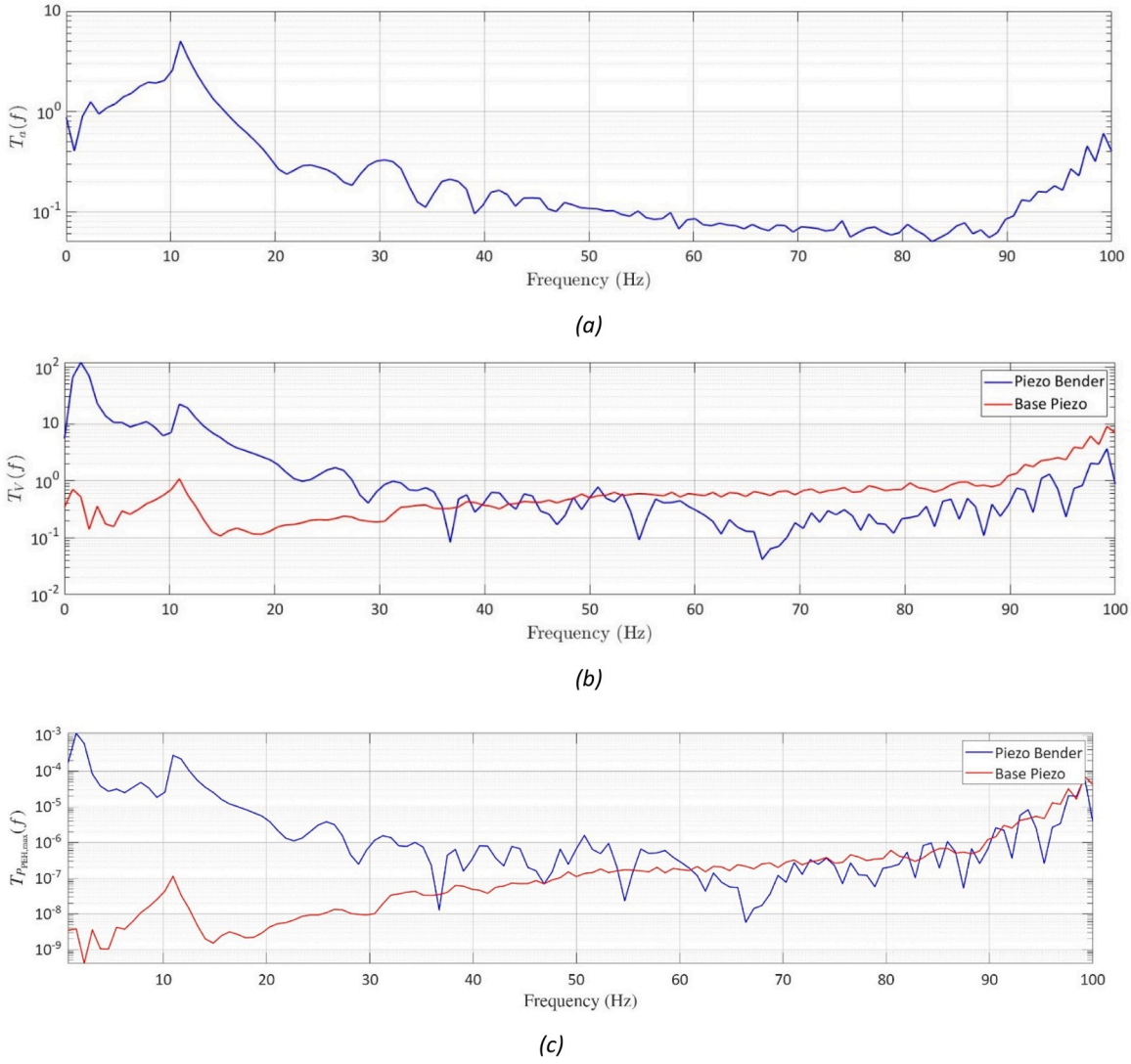

Fig. 13. Transfer Functions for V-Structure normalized per input acceleration "g" **(a)** upper plate acceleration, **(b)** PB and PZT Voltage ($\frac{V}{g}$), and **(c)** PB and PZT maximum average power ($\frac{W}{g}$).

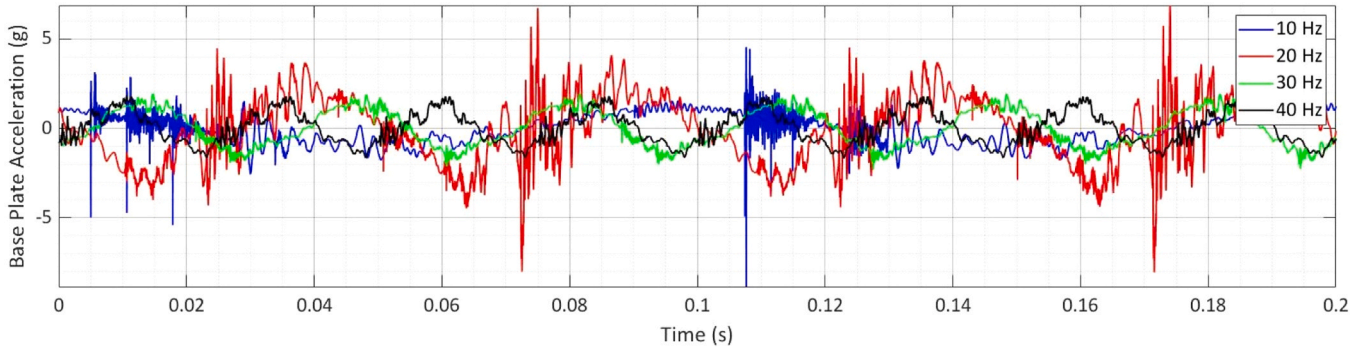

(a)

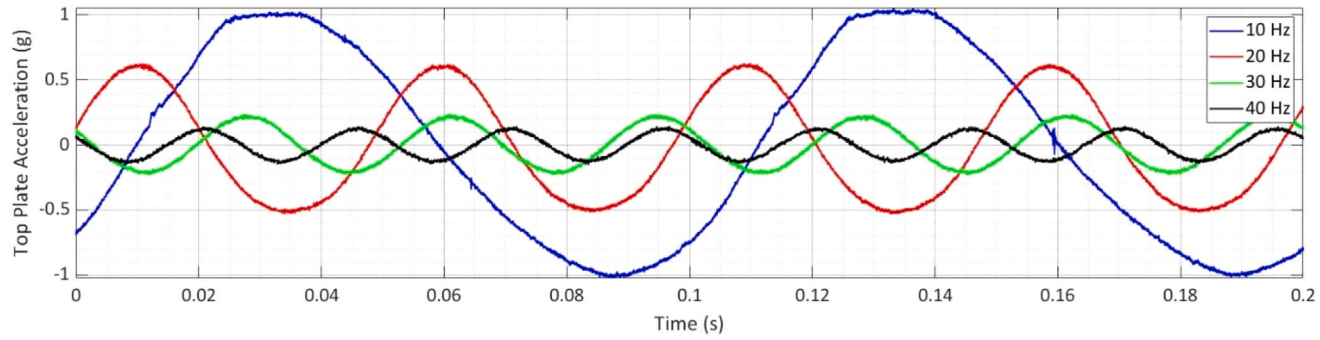

(b)

Fig. 14. Acceleration of the **(a)** Base Plate, and **(b)** Top Plate for V-Structure.

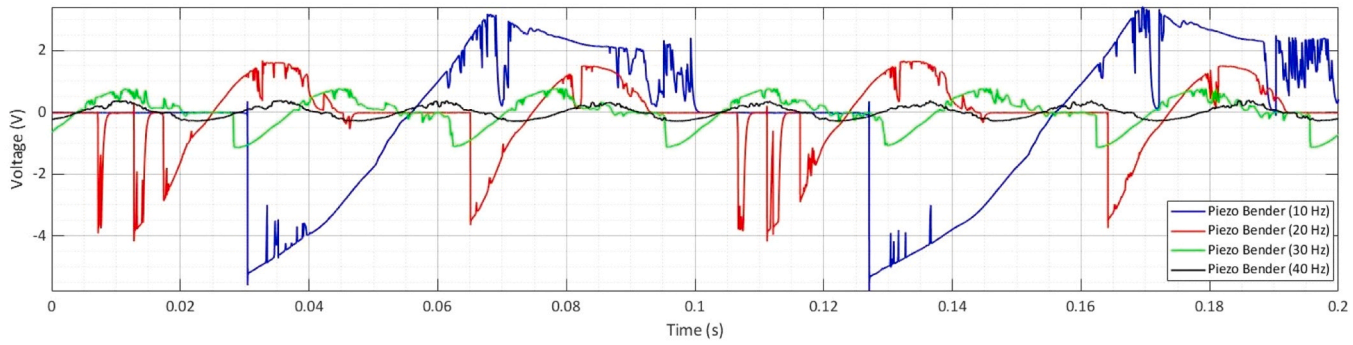

(a)

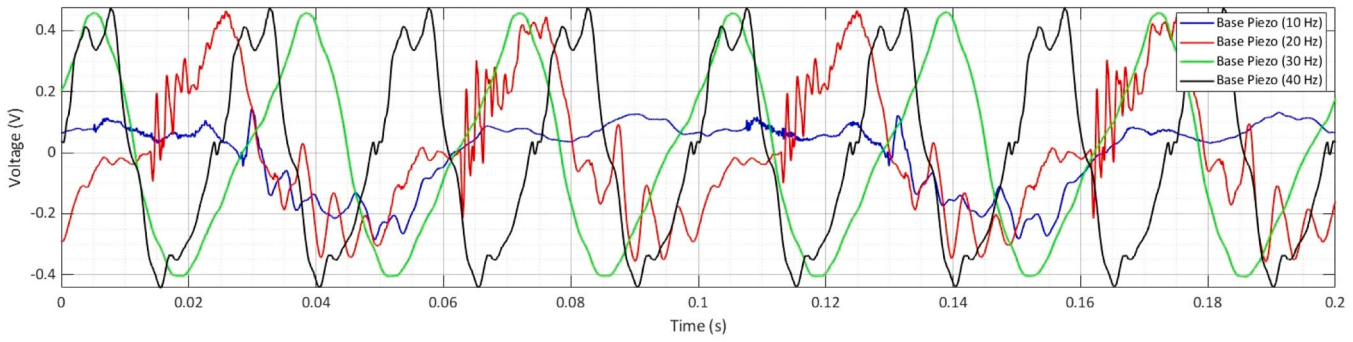

(b)

Fig. 15. Voltages of **(a)** PB and **(b)** base PZT at varying frequencies (V-Structure).

substantial difference in overall energy generation performance.

To further analyze the structure's behavior at different frequencies, we applied harmonic base vibrations at 10, 20, 30, and 40 Hz, and recorded the time-domain responses from 0 to 0.2 s. Fig. 14 presents the accelerations of the base plate and top plate at these frequencies. The base plate vibrations are not purely harmonic and include higher-frequency components due to the experimental setup. However, Fig. 14***b*** shows that the higher-frequency components are effectively damped in the top plate vibrations due to the vibration isolation feature of the metamaterial, resulting in a more harmonic response compared to the base plate, where the high-frequency components are more pronounced. Moreover, comparing Fig. 14***a*** and Fig. 14***b*** reveals that at 10 Hz, the damping of the main frequency component (10 Hz) is not evident, but as the frequency increases to 20, 30, and 40 Hz, the damping of the primary frequency components becomes progressively more effective.

Fig. 15 shows the voltages generated by the PB and the PZT. As depicted, the PB generates significantly higher voltages compared to the PZT. However, as the base vibration frequency increases from 10 to 40 Hz (Fig. 13***b***), the voltage output of the PB decreases, while the voltage of the PZT increases. This behavior is due to the PB being embedded within the lattice structure, which effectively damps higher-frequency vibrations, leaving less energy for the PB to generate. However, the PZT at the base receive the vibrations directly before they pass through the lattice structure, allowing them to generate more energy at higher frequencies.

3.2.2. *H structure*

Fig. 16 presents the transfer functions of the "H-structure", with base plate acceleration "g" as the input, upper plate acceleration (Fig. 16***a***),

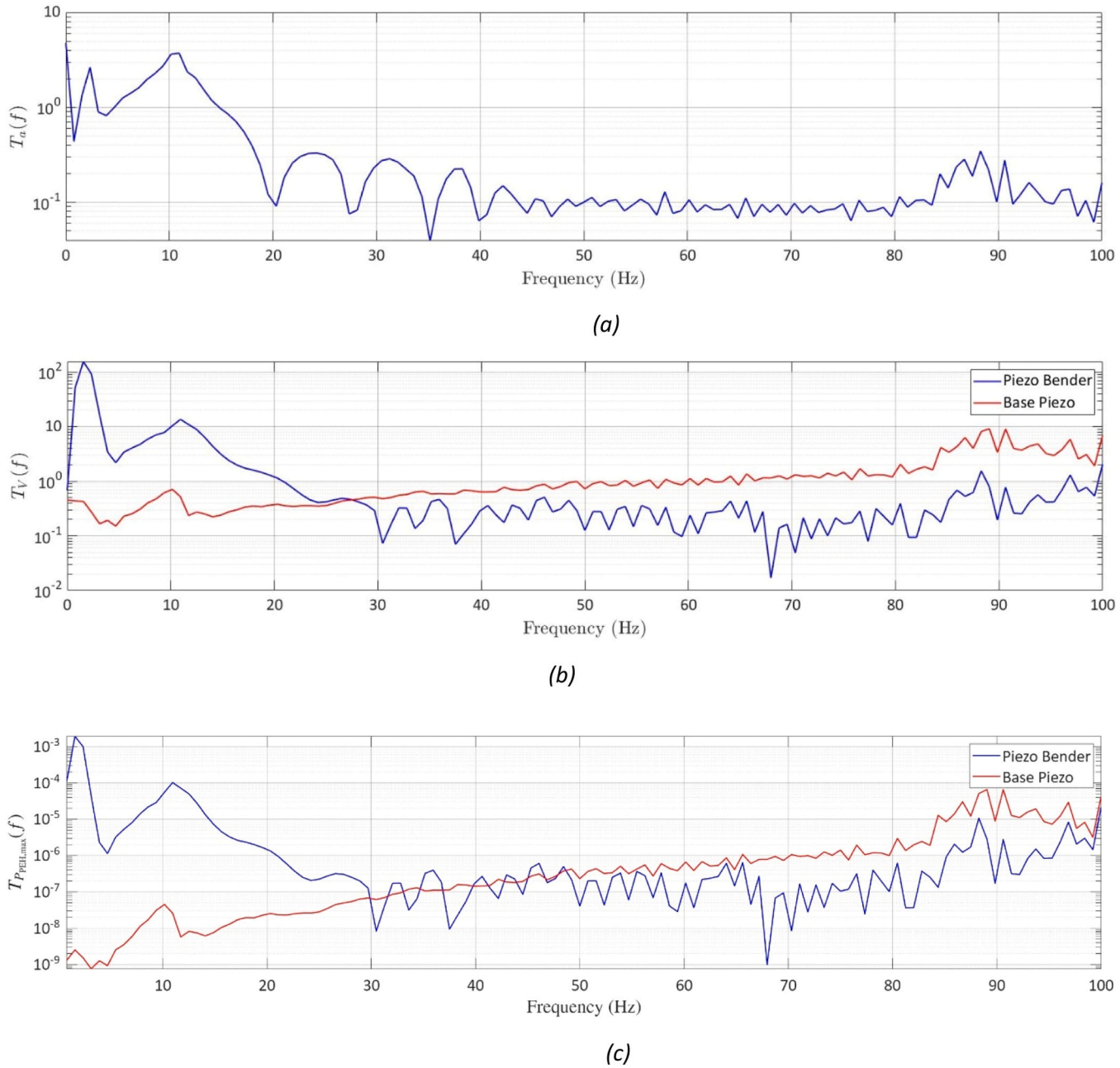

Fig. 16. Transfer Functions for H-Structure normalized per input acceleration "g" **(a)** upper plate acceleration, **(b)** PB and PZT voltage generation ($\frac{V}{g}$), and **(c)** PB and PZT maximum average power ($\frac{W}{g}$).

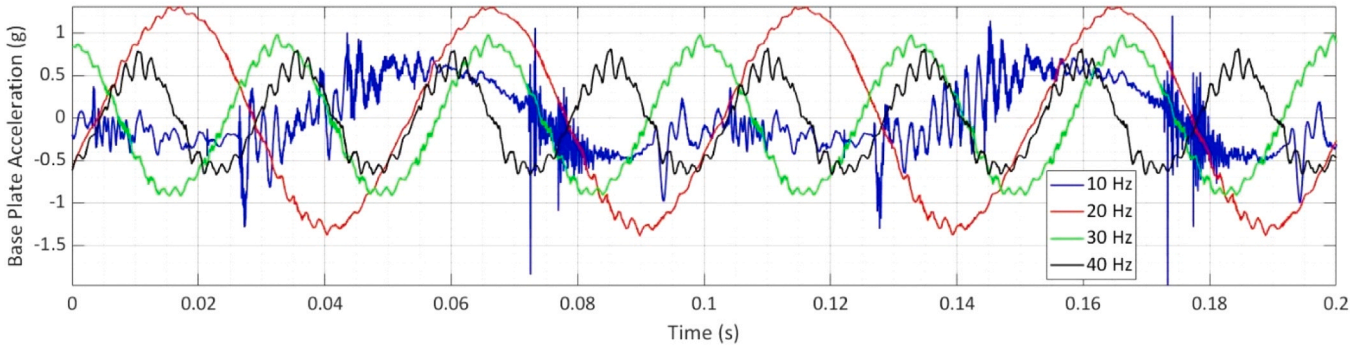

(a)

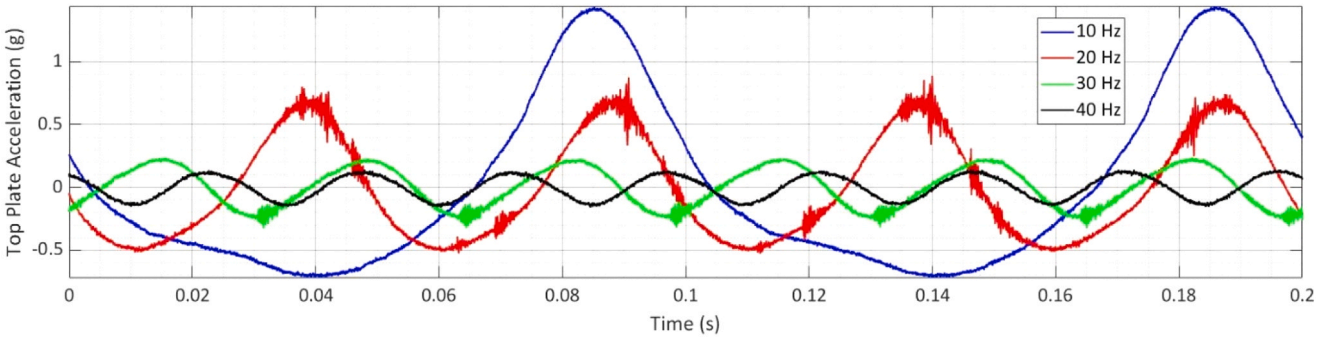

(b)

Fig. 17. Acceleration of the **(a)** base plate and **(b)** top plate (H-Structure).

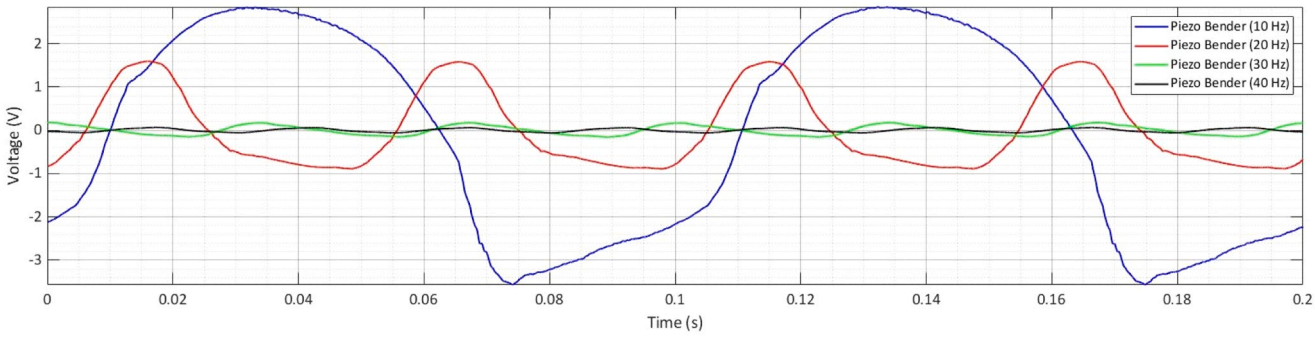

(a)

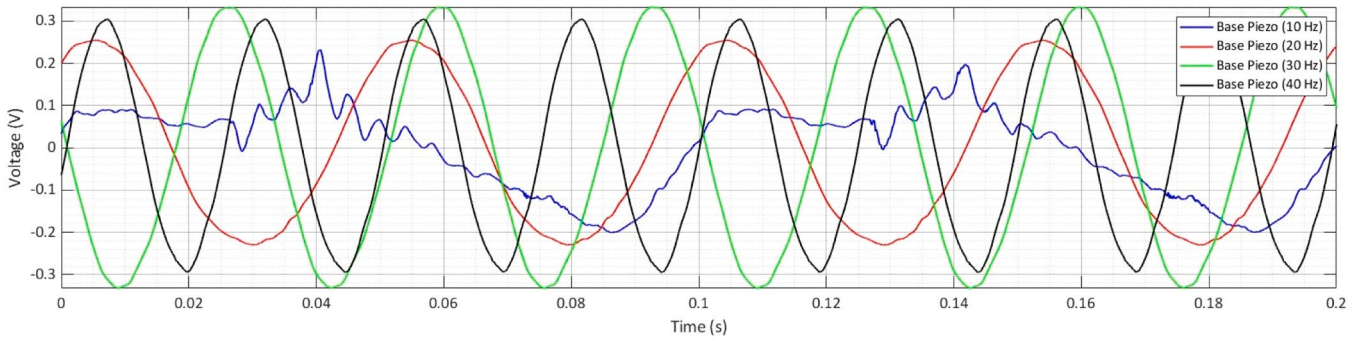

(b)

Fig. 18. Voltages of **(a)** PB and **(b)** PZT at varying frequencies (H-Structure).

the piezoelectric voltages (Fig. 16***b***), and maximum average power (raw power) (Fig. 16***c***) as outputs. Fig. 16***a*** demonstrates that the "H-structure" effectively dampens vibrations beyond 15 Hz, where the transfer function drops below one. Additionally, Fig. 16***b*** and Fig. 16***c*** compare the PB's and PZT's generated voltages and maximum average power. It shows that the PB generates higher voltages below 27 Hz. However, beyond 15 Hz, the base PZT's voltage output increases and surpasses that of the PB around 27 Hz, while the generated power remains comparable up to approximately 50 Hz. Beyond this point, the PZT also exceeds power output, indicating a shift in energy generation efficiency at higher frequencies. The PB in the "V-structure" outperforms the PZT over a wider frequency range compared to the H-structure, as in the "H-structure", the PB is positioned closer to the top surface of the lattice, where the vibrations are almost fully damped.

Fig. 17 shows the time-domain acceleration of the H-structure under harmonic base vibrations at 10, 20, 30, and 40 Hz. Similar to the "V-Structure" ***(***Fig. 14***)***, the accelerations of the base plate ***(***Fig. 17***a)*** and top plate ***(***Fig. 17***b)*** reveal that higher-frequency components are present in the base vibrations due to the setup, but these components are effectively damped in the top plate, resulting in a more harmonic response. At 10 Hz, damping of the primary frequency component (10 Hz) is ineffective, but as the frequency increases to 20, 30, and 40 Hz, the damping becomes progressively more effective due to lattice vibration isolation performance. These results reveal the effectiveness of the "H-structure" in damping and isolating higher-frequency vibrations.

Fig. 18 shows the voltages generated by the PB ***(***Fig. 18***a)*** and PZT ***(***Fig. 18***b)*** in the "H-structure". Initially, the PB exhibits higher voltage output than the PZT, but as the base plate vibration frequency increases from 10 to 40 Hz ***(***Fig. 16***b)***, the PB's voltage output declines. In contrast, the PZT's voltage increases as the frequency shifts from 10 to 20 Hz, and then it demonstrates more consistent amplitudes. This behavior is due to the PB's location near the top of the structure, where effective vibration isolation at higher frequencies reduces the available energy for generation. Meanwhile, the PZT, which directly receives vibrations from the base plate, generates more energy at higher frequencies.

4. Potential applications

Given the power demands of common sensors [67], typically in the range of 10–1000 μW, the energy generated from a single piezo bender and PZT in this research is already within the usable range for intermittent operation (piezo bender outputting power approximately 600–700 $\frac{\mu W}{g}$ at a low frequency of 15 Hz, while PZT outputting power approximately 800 $\frac{\mu W}{g}$ at a high frequency of 90 Hz, see Figs. 13 and 16). Furthermore, the structural design allows for multiple piezo benders to be embedded in a whole layer of the lattice, enabling scalable power output for more demanding applications. It is also worth mentioning that the findings of this research are material-independent, as discussed in the Appendix and shown in Fig. 20. Therefore, this research can have many potential applications in multiple engineering fields. In civil engineering, the proposed hybrid metamaterials can be embedded in bridge supports or joints to mitigate low-frequency vibrations and enable self-powered sensors for real-time structural health monitoring, see Fig. 19***a***. In the bike wheel, the lattice structure can dampen vibrations and generate electricity to power onboard lighting or sensors, see Fig. 19***b***. For the car seat application, it enhances passengers' comfort by

Fig. 19. The applications of the proposed smart metamaterials in **(a)** bridge supports [68], **(b)** bike wheels [69], **(c)** car seats, **(d)** glowing shoes, **(e)** smart wearables, **(f)** treadmills [70], and **(g)** scooters [71]. (Fig. 19 (b), (f), and (g) are reproduced with permissions from Pexels and Pixabay. These figures are free to use and modify based on the licenses of Pexels and Pixabay.).

isolating vibrations while potentially generating energy to charge internal vehicle systems, see Fig. 19***c***. The glowing shoes and treadmill applications, Fig. 19***d, e,*** and ***f***, demonstrate the versatility of QZS lattice structures in wearable and fitness technologies. These structures reduce shock impacts during walking or running, preventing knee injuries, while simultaneously generating energy from the user's motion, which can be used to power auxiliary devices or displays. The scooter demonstrates how these lattice structures can be applied in suspension systems to provide a smoother ride while generating electricity for lights or other functions, see Fig. 19***g***. Such energy generation systems are particularly beneficial for portable devices, reducing dependence on external power sources. The adaptability of the smart lattice structures makes them suitable for both small-scale wearables and larger automotive or mobility platforms, representing a novel integration of mechanical and energy functionalities and showcasing the future potential of smart metamaterials in engineering.

5. Conclusions

This study focuses on developing additively manufactured TPU-based multi-functional sinusoidal metamaterials tailored for simultaneous vibration isolation and electricity generation applications. Conventional auxetic re-entrant unit cells are reformulated by integrating curved patterns. The key findings are summarized as follows.

- A novel QZS mechanism is achieved by inducing nonlinearity through the buckling of vertical beams under compression loads.
- The curved design of the unit cells leads to the multi-stiffness property of the unit cells. This means the higher the curvature, the lower the stiffness.
- Hybrid designs containing low and high-stiffness unit cells, called "H" and "V" structures, are proposed to provide global stability through high-stiffness components while allowing localized buckling in low-stiffness sections to maintain QZS properties.
- Hybrid lattice designs ("H" and "V" structures) exhibit effective vibration isolation above 15 Hz due to their unique deformation mechanisms.
- Two types of piezoelectric materials, namely Lead zirconate titanate (PZT) and piezo bender (PB), are utilized for electricity generation.
- The PB, embedded within the lattice in the through-depth direction, generates up to 3 volts due to significant bending forces caused by local buckling of the walls.
- The PB generates power up to 600–700 microwatts per gravity ($\frac{\mu W}{g}$) at a low frequency of 15 Hz, where vibration isolation arises.
- The PZT, placed on a stiffer PLA semi-honeycomb structure, produces up to 500 millivolts of electricity and a maximum output power of around 800 $\frac{\mu W}{g}$ at a high frequency of 90 Hz.

Our proposed lattice structures offer improved functionality for various applications as they are material-independent. In civil infrastructure, these structures can be embedded in bridge bearings or expansion joints to attenuate low-frequency vibrations and power wireless monitoring sensors. In car seats, they isolate vibrations to enhance passenger comfort while simultaneously generating electricity to power up built-in electronics. For bikes and scooters, they enhance suspension systems, ensuring smoother rides and supplying energy for onboard devices. Furthermore, they can be incorporated into smart shoes to reduce impact forces and generate power for integrated technologies.

CRediT authorship contribution statement

Ramin Hamzehei: Writing – original draft, Validation, Software, Methodology, Investigation, Formal analysis, Conceptualization. **Mahdi Alaei Varnosfaderani:** Writing – original draft, Validation, Software, Methodology, Investigation, Formal analysis. **Mahdi Bodaghi:** Writing – review & editing, Supervision, Software, Methodology, Investigation. **Nan Wu:** Writing – review & editing, Supervision, Methodology, Conceptualization.

Declaration of Competing Interest

The authors declare that they have no known competing financial interests or personal relationships that could have appeared to influence the work reported in this paper.

Acknowledgments

The authors would like to gratefully acknowledge the support by the University of Manitoba, Research Manitoba [RMB IPC #5572], National Sciences and Engineering Research Council of Canada [NSERC, RGPIN 2021–03356], Mitacs Accelerate [IT45842], and the UK Engineering and Physical Sciences Research Council (EPSRC) [EP/Y011457/1].

Appendix

Materials diversity effects on the mechanical response of the hybrid lattice structures

To ensure that the desired vibration isolation effect with clear QZS property is geometry-dependent, the "H" and "V" structures are additively manufactured via PLA silk material, showing elastic-plastic behavior (see Fig. 20a). As can be seen from Fig. 20b, the deformation patterns happen at the lower-stiffness unit cells "C" first, resulting in local buckling of the walls in low-stiffness unit cells, see Fig. 20b. This leads to an introduction of non-linearity to the system and a simultaneous QZS property, see Fig. 20c. Therefore, according to Section 3.1 and the current discussion here, the QZS property arises from lattice structural design rather than material.

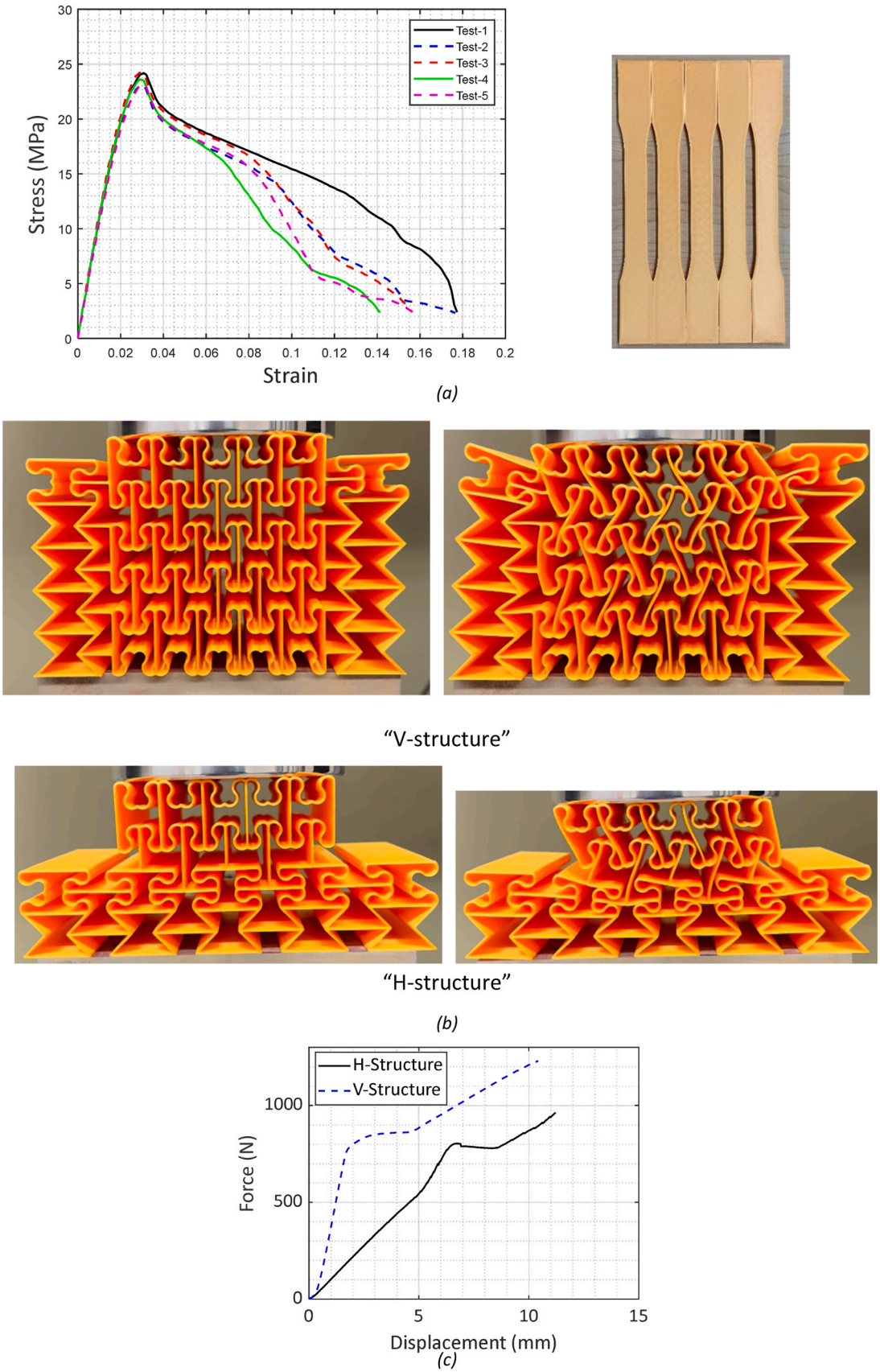

Fig. 20. ***(a)*** mechanical property of PLA silk, ***(b)*** deformation patterns of lattice structures "V" and "H", and ***(c)*** the corresponding force-displacement relation obtained from the experiment

Data availability

Data will be made available on request.

References

[1] Lim T-C. A reconfigurable metamaterial using trapeziums and triangles with alternative connectivity. Eur J MechA/Solids 2024;106:105336.
[2] Onyibo EC, Gazioglu A, Ahmed AA, Ameer AAA, Abdelrahman ME, Oladipupo OA, et al. Experimental and numerical investigations on uniaxial-stress ductility failure of additive manufactured lattice structures based on frequency fatigue technique. Acta Mech 2025;236(1):37–57.
[3] Zhang Z, Wen Q, Li P, Hu H. Application of double arrowhead auxetic honeycomb structure in displacement measurement. Sens Actuators A Phys 2022;333:113218.
[4] Li B, Liang W, Zhang L, Ren F, Xuan F. TPU/CNTs flexible strain sensor with auxetic structure via a novel hybrid manufacturing process of fused deposition modeling 3D printing and ultrasonic cavitation-enabled treatment. Sens Actuators A Phys 2022;340:113526.
[5] Jiang T, Han Q, Li C. Design and compression-induced bandgap evolution of novel polygonal negative stiffness metamaterials. Int J Mech Sci 2024;261:108658.
[6] Tan X, Zhu S, Wang B, Kadic M. Tuning negative stiffness mechanical metamaterial's snap-through behavior with a series-connected spring. Eur J MechA/Solids 2024;107:105382.
[7] Zhang Q, Sun Y. Novel metamaterial structures with negative thermal expansion and tunable mechanical properties. Int J Mech Sci 2024;261:108692.
[8] Zhang Q, Sun Y. A series of auxetic metamaterials with negative thermal expansion based on L-shaped microstructures. ThinWalled Struct 2024;197:111596.
[9] Wang L-Y, Liu H-T, Liu K-J. 3D bi-directional auxetic square metastructure with programmable thermal expansion and poisson's ratio. ThinWalled Struct 2024; 205:112569.
[10] Ma R, Liu L, Wyman O, Pasini D. Programming polymorphable yet stiff truss metamaterials in response to temperature. Appl Mater Today 2022;27:101432.
[11] Hamzehei R, Bodaghi M, Wu N. 3D-printed highly stretchable curvy sandwich metamaterials with superior fracture resistance and energy absorption. Int J Solids Struct 2024;286:112570.
[12] Hamzehei R, Bodaghi M, Wu N. Bio-inspired design and 4D printing of multi-stiffness wavy metamaterial energy absorbers/dissipators with shape recovery features. Eng Struct 2025;327:119538.
[13] Hamzehei R, Bodaghi M, Wu N. Mastering the art of designing mechanical metamaterials with quasi-zero stiffness for passive vibration isolation: a review. Smart Mater Struct 2024;33(8):083001.
[14] Li Y, Baker E, Reissman T, Sun C, Liu WK. Design of mechanical metamaterials for simultaneous vibration isolation and energy harvesting. Appl Phys Lett 2017;111 (25).
[15] Fu T, Rao E, Rabczuk T. Sound transmission loss and energy absorbing performance of stiffened doubly-curved shells with corrugated-honeycomb hybrid cores. Eur J MechA/Solids 2024;107:105386.
[16] Ji G, Huber J. Recent progress in acoustic metamaterials and active piezoelectric acoustic metamaterials-a review. Appl Mater Today 2022;26:101260.
[17] Zhou Y, Li Y, Jiang D, Chen Y, Xie YM, Jia L-J. In-plane impact behavior of 3D-printed auxetic stainless honeycombs. Eng Struct 2022;266:114656.
[18] Li C, Shen H-S, Yang J. Multi-scale modeling and numerical analysis of sandwich beams with FG auxetic 3D lattice cores and GRC face sheets subjected to drop-weight impacts. Eng Struct 2022;265:114486.
[19] Tao R, Shi J, Granier F, Moeini M, Akbarzadeh A, Therriault D. Multi-material fused filament fabrication of flexible 3D piezoelectric nanocomposite lattices for pressure sensing and energy harvesting applications. Appl Mater Today 2022;29: 101596.
[20] Fang S, Du H, Yan T, Chen K, Li Z, Ma X, et al. Theoretical and experimental investigation on the advantages of auxetic nonlinear vortex-induced vibration energy harvesting. Appl Energy 2024;356:122395.
[21] Fang S, Chen K, Lai Z, Zhou S, Liao W-H. Analysis and experiment of auxetic centrifugal softening impact energy harvesting from ultra-low-frequency rotational excitations. Appl Energy 2023;331:120355.
[22] Hu G, Tang L, Liang J, Lan C, Das R. Acoustic-elastic metamaterials and phononic crystals for energy harvesting: a review. Smart Mater Struct 2021;30(8):085025.
[23] Kumar R, Kumar M, Chohan JS, Kumar S. Overview on metamaterial: history, types and applications. Mater Today Proc 2022;56:3016–24.
[24] Dalela S, Balaji P, Jena D. A review on application of mechanical metamaterials for vibration control. Mech Adv Mater Struct 2022;29(22):3237–62.
[25] Bahl S, Nagar H, Singh I, Sehgal S. Smart materials types, properties and applications: a review. Mater Today Proc 2020;28:1302–6.
[26] Joshi S, Rawat K, Rajamohan V, Mathew AT, Koziol K, Thakur VK, ASS B. 4D printing of materials for the future: opportunities and challenges. Appl Mater Today 2020;18:100490.
[27] Akbar I, El Hadrouz M, El Mansori M, Tarfaoui M. Thermomechanical shape memory testing of 4D printed novel material rhombus-shape structure. Appl Mater Today 2023;33:101876.
[28] Ashtiani M, Hashemabadi S, Ghaffari A. A review on the magnetorheological fluid preparation and stabilization. J Magn Magn Mater 2015;374:716–30.
[29] Viet N, Wu N, Wang Q. A review on energy harvesting from ocean waves by piezoelectric technology. J Model Mech Mater 2017;1(2).
[30] Delbariani-Nejad A, Xiong Y. Probabilistic investigation of piezoelectric application for reliability enhancement of composite laminates under edge delamination. Compos Struct 2024;349:118528.
[31] Alshenawy R, Sahmani S, Safaei B, Elmoghazy Y, Al-Alwan A, Al Nuwairan M. Three-dimensional nonlinear stability analysis of axial-thermal-electrical loaded FG piezoelectric microshells via MKM strain gradient formulations. Appl Math Comput 2023;439:127623.
[32] Gao W, Hu J, Qin Z, Chu F. Flexural wave manipulation in perforated metamaterial plates with acoustic black holes interconnected by piezoelectric studs. Compos Struct 2023;321:117224.
[33] Zhu Q, Zhu L, Wang Z, Zhang X, Li Q, Han Q, et al. Hybrid triboelectric-piezoelectric nanogenerator assisted intelligent condition monitoring for aero-engine pipeline system. Chem Eng J 2025:165121.
[34] Liu H, Sahmani S, Safaei B. Nonlinear buckling mode transition analysis in nonlocal couple stress-based stability of FG piezoelectric nanoshells under thermo-electromechanical load. Mech Adv Mater Struct 2023;30(16):3385–405.
[35] Rao S, Yap F. Mechanical vibrations addison. Wesley Publishing Co. United States of America; 1995.
[36] Ji J, Luo Q, Ye K. Vibration control based metamaterials and origami structures: a state-of-the-art review. Mech Syst Signal Process 2021;161:107945.
[37] Wu Z, Liu W, Li F, Zhang C. Band-gap property of a novel elastic metamaterial beam with X-shaped local resonators. Mech Syst Signal Process 2019;134:106357.
[38] Amendola A, Benzoni G, Fraternali F. Non-linear elastic response of layered structures, alternating pentamode lattices and confinement plates. Composites Part B Engineering 2017;115:117–23.
[39] Matlack KH, Bauhofer A, Krödel S, Palermo A, Daraio C. Composite 3D-printed metastructures for low-frequency and broadband vibration absorption. Proc Natl Acad Sci 2016;113(30):8386–90.
[40] Zhang Q, Guo D, Hu G. Tailored mechanical metamaterials with programmable quasi-zero-stiffness features for full-band vibration isolation. Adv Funct Mater 2021;31(33):2101428.
[41] Liu J, Wang Y, Yang S, Sun T, Yang M, Niu W. Customized quasi-zero-stiffness metamaterials for ultra-low frequency broadband vibration isolation. Int J Mech Sci 2024;269:108958.
[42] Liu W, Wu L, Zhang J, Sun J, Zhou J. Metamaterial springs for low-frequency vibration isolation. J Mater 2025;11(1):100884.
[43] Liang K, Jing Y, Zhang X. Design of broad quasi-zero stiffness platform metamaterials for vibration isolation. Int J Mech Sci 2024;281:109691.
[44] Liu W, Wu L, Sun J, Zhou J. Origami-inspired quasi-zero stiffness metamaterials for low-frequency multi-direction vibration isolation. Appl Phys Lett 2023;123(8).
[45] Dalela S, Ps B, Jena DP, Leblouba M. A tunable metamaterial using a single beam element with quasi-zero-stiffness characteristics for low-frequency vibration isolation. J Vib Control 2024;30(15-16):3641–58.
[46] Huo K, Yuan Z, Zhou G, Mu R, Wang K, Zhao H. Modeling of programmable low-frequency isolator with quasi-zero stiffness metamaterials. Acta Mech 2024;235(5): 2919–44.
[47] Zhao J, Zhou G, Zhang D, Kovacic I, Zhu R, Hu H. Integrated design of a lightweight metastructure for broadband vibration isolation. Int J Mech Sci 2023; 244:108069.
[48] Zhou J, Zhou J, Pan H, Wang K, Cai C, Wen G. Multi-layer quasi-zero-stiffness meta-structure for high-efficiency vibration isolation at low frequency. Appl Math Mech 2024;45(7):1189–208.
[49] Fan H, Yang L, Tian Y, Wang Z. Design of metastructures with quasi-zero dynamic stiffness for vibration isolation. Compos Struct 2020;243:112244.
[50] Chen K, Fang S, Gao Q, Zou D, Cao J, Liao W-H. Enhancing power output of piezoelectric energy harvesting by gradient auxetic structures. Appl Phys Lett 2022;120(10).
[51] Li Q, Kuang Y, Zhu M. Auxetic piezoelectric energy harvesters for increased electric power output. Aip Adv 2017;7(1).
[52] Farhangdoust S, Georgeson G, Ihn J-B, Chang F-K. Kirigami auxetic structure for high efficiency power harvesting in self-powered and wireless structural health monitoring systems. Smart Mater Struct 2020;30(1):015037.
[53] Fey T, Eichhorn F, Han G, Ebert K, Wegener M, Roosen A, et al. Mechanical and electrical strain response of a piezoelectric auxetic PZT lattice structure. Smart Mater Struct 2015;25(1):015017.
[54] Eghbali P, Younesian D, Farhangdoust S. Enhancement of piezoelectric vibration energy harvesting with auxetic boosters. Int J Energy Res 2020;44(2):1179–90.
[55] Ferguson WJ, Kuang Y, Evans KE, Smith CW, Zhu M. Auxetic structure for increased power output of strain vibration energy harvester. Sens Actuators A Phys 2018;282:90–6.
[56] Chen K, Fang S, Gao Q, Zou D, Cao J, Liao W-H. An enhanced nonlinear piezoelectric energy harvester with multiple rotating square unit cells. Mech Syst Signal Process 2022;173:109065.
[57] Ichige R, Kuriyama N, Umino Y, Tsukamoto T, Suzuki T. Size optimization of metamaterial structure for elastic layer of a piezoelectric vibration energy harvester. Sens Actuators A Phys 2021;318:112488.
[58] Tabak A, Safaei B, Memarzadeh A, Arman S, Kizilors C. An extensive review of piezoelectric energy-harvesting structures utilizing auxetic materials. J Vib Eng Technol 2024;12(3):3155–92.
[59] Anigbogu W, Bardaweel H. A Metamaterial-Inspired structure for simultaneous vibration attenuation and energy harvesting. Shock Vib 2020;2020(1):4063025.
[60] Banerjee P, Dalela S, Balaji P, Murugan S, Kumaraswamidhas L. Simultaneous vibration isolation and energy harvesting using quasi-zero-stiffness-based metastructure. Acta Mech 2023;234(8):3337–59.

[61] Hyun J, Jung J, Park J, Choi W, Kim M. Simultaneous low-frequency vibration isolation and energy harvesting via attachable metamaterials. Nano Converg 2024; 11(1):38.
[62] Xu X, Wu Q, Pang Y, Cao Y, Fang Y, Huang G, Cao C. Multifunctional metamaterials for energy harvesting and vibration control. Adv Funct Mater 2022; 32(7):2107896.
[63] Qi HJ, Boyce MC. Stress–strain behavior of thermoplastic polyurethanes. Mech Mater 2005;37(8):817–39.
[64] Anand Kumar S, Shivraj Narayan Y. Tensile testing and evaluation of 3D-printed PLA specimens as per ASTM D638 type IV standard. Innovative Design, Analysis and Development Practices in Aerospace and Automotive Engineering (I-DAD 2018), 2. Springer; 2018. p. 79–95.
[65] [Available from: ⟨https://www.piezodrive.com/actuators/piezo-bender-actuators/⟩.
[66] Pandiev I, Tomchev N, Kurtev N, Aleksandrova M. Analysis of the methods for realization of low-power piezoelectric energy harvesting circuits for wearable battery-free power supply devices. Appl Sci 2024;14(11):4792.
[67] Hidalgo-Leon R, Urquizo J, Silva CE, Silva-Leon J, Wu J, Singh P, Soriano G. Powering nodes of wireless sensor networks with energy harvesters for intelligent buildings: a review. Energy Rep 2022;8:3809–26.
[68] Bridge [Available from: ⟨https://www.pexels.com/photo/grey-concrete-bridge-on-body-of-water-under-blue-and-white-sky-during-daytime-128362/⟩.
[69] Bike [Available from: ⟨https://www.pexels.com/photo/rear-wheel-of-bike-illuminated-in-blue-13061204/⟩.
[70] Treadmill [Available from: ⟨https://pixabay.com/photos/fitness-treadmill-running-957115/⟩.
[71] Scooter [Available from: ⟨https://pixabay.com/photos/scooter-e-bike-e-scooter-city-4953510/⟩.